

Intermediate report on the ITER service contract
C4T/09/71/OLT CHD/DIAGNOSTIC: “Study on effective
fluxes to the first mirror which face the plasma directly”

V. Kotov, D. Reiter, Forschungszentrum Jülich GmbH, IEF-4 Plasma Physik
with contributions from A. Litnovsky, P. Börner, S. Wiesen and A. Kirschner

April 9, 2010

Contents

1	Introduction	3
2	The model	3
3	Technical aspects	5
4	Preliminary results	8
4.1	Equatorial Port	8
4.2	Upper Port	10
4.3	Helium	12
4.4	Divertor	12
4.5	Summary	13
5	Outstanding issues and plans	15
6	Appendix A: Sensitivity assessment	17
6.1	Verification	17
6.2	Sensitivity with respect to the applied model	18
6.3	Sensitivity with respect to the core plasma profiles	18
6.4	The effect of magnetic configuration	19
7	Appendix B: EIRGRID and EIRMAP data format and libraries	22
7.1	General structure	22
7.2	EIRGRID object (module eirgrid.f)	23
7.2.1	EIRGRID: data	23
7.2.2	EIRGRID: methods	24
7.3	EIRMAP object (module eirmap.f)	25
7.3.1	EIRMAP: data	25
7.3.2	EIRMAP: methods	25
7.4	Grid-type specific routines (eirgrid_interf.f)	26
7.5	Subroutines which create a grid object	26
8	Appendix C: Grid generator COREGRID	27
8.1	Theoretical background	27
8.2	Technical description	30
9	Appendix D: The spectrum calculation option in EIRENE	31
9.1	Technical description	31
9.2	Instruction for Users: Input and Output	31
9.3	Test problems	33

Abstract

The report contains first estimates of the incident neutral fluxes and spectra in ITER required for evaluating the life time of the first mirrors of the optical diagnostics. The calculations are based on a series of B2-EIRENE simulations of the ITER SOL plasma carried out by IO. The applied model and its implementation is described. Particular emphasis is made on combining the SOL and core plasma regions in a single simulation in order to calculate realistic spectra of the high energetic (supra-thermal) particles. Worst cases for both erosion of bulk material and deposition of impurities have been identified. The results suggest that at both equatorial and upper ports erosion of the Mo mirrors due to DT atoms will not exceed $10 \mu\text{m}/\text{year}$ (1 ITER year=1000 discharges \times 400 sec). Deduced erosion and deposition rates of impurities (represented by C) at the first wall are always of the same order of magnitude. This makes reliable predictions of the net effect difficult (taking into account all the model uncertainties). Net erosion conditions at the first wall are likely in the equatorial port. In the upper port region either net erosion or net deposition may occur, depending on not yet resolved details. Net deposition is expected in the divertor sub-dome region. Further improvements of the model to be carried out in the next project phase are outlined.

1 Introduction

This report is organized as follows: in section 2 the simulation model employed here is described. Section 3 contains merely technical information regarding code details, and may be skipped if only the physical results are of interest. The results obtained in the first project phase are described in Section 4.

2 The model

SOL plasma parameters for the simulations in the present work were taken from the series of B2-EIRENE simulations listed in Table 2. These simulations are made for the nominal ITER discharges with 500 MW fusion power and 80-120 MW SOL power. Magnetic equilibrium and divertor configuration F57 (2009 reference). More details can be found in [1]. Both plasma fueling with gas puff (located in the upper port) and pellet injection (cases 1679, 1735) are considered. The model plasma consists of all ionized states of D, He and C. Here D represents both D and T. Carbon is an intrinsic impurity coming from the divertor and first wall sputtering. The presence of carbon ensures that 40-70 % of the SOL input power is radiated leading to edge plasma solutions with partially detached divertor. There are no numerically fully converged simulations for the F57 configuration with seeded impurities available yet. However, the solution will most likely be similar if the radiated fraction is the same.

All B2-EIRENE simulations are made on assumption that the wall is coated by deposited carbon. This assumption is typically used because in this case the calculated operational scalings are close to those obtained with the so called “realistic wall model” of B2-EIRENE runs for ITER, which takes into account net deposition of C (deposition minus erosion) [2]. For the purpose of the present study it could have been better to use a more realistic assumption of a Be-coated wall. From the experience of the previous calculations however [3] it is known that plasma parameters do not significantly change when switching from C to Be wall.

Fluxes, energy- and angular spectra of the incident particles and sputtered fluxes are calculated by the kinetic Monte-Carlo transport code EIRENE [4] on fixed plasma backgrounds. A rather similar approach (although, with a less complete model at that time) was used in the paper by Verbeek et al. [5] there the Neutral Particle Analyzer measurements made in ASDEX-Upgrade were satisfactorily well reproduced by EIRENE calculations.

It is expected that mirrors made of refractory metals (e.g. Mo) will be sputtered mainly by energetic neutral particles with energies ~ 1 keV and more. The main source of such particles will be charge exchange and elastic processes in the hot plasma inside the magnetic separatrix. The simulation model has to, therefore, include a proper description of the core plasma region as well. In order to achieve that in the Monte-Carlo calculations presented in this report the B2 grid inside separatrix was replaced by a grid defined in the entire core domain, see next Section.

Plasma parameters inside separatrix are taken from the 1D transport simulations made with ASTRA code by IO as found in the document [Yu. Gribov, T. Casper, A. Polevoi, ITER IDM ITER.D.2V2XYR]. The radial profiles are shown in Appendix A, Section 6.3. It is assumed that

Table 1: List of B2-EIRENE simulations used as input for the modelling

Case	P_{SOL} MW	Γ_{puff} $10e22 \text{ s}^{-1}$	n_s^e $1e19 \text{ m}^{-3}$	p_{PFR} Pa	q_{pk} MW/m^2	f_{rad} %	T_s^e eV	T_s^i eV
1511	100	2.25	3.7	2.6	11	47	336	202
1542	100	15.5	3.3	10	4.6	67	330	199
1568	80	1.17	3.3	2.0	8.7	44	323	190
1597	80	9.1	2.9	6.8	3.9	64	311	186
1640	120	6.4	4.0	5.0	9.9	55	350	211
1639	120	22	3.7	13	5.6	70	350	211
1679	100	Core: 5.4	4.1	4.1	8.0	51	301	190
1735	100	Core: 5.4 Puff: 7.9	3.7	8.7	5.2	65	306	192

P_{SOL} is the SOL input power;

Γ_{puff} is the gas puffing rate;

n_s^e is the separatrix electron density at the outer midplane;

p_{PFR} is the average neutral gas pressure in the divertor;

q_{pk} is the peak target heat flux;

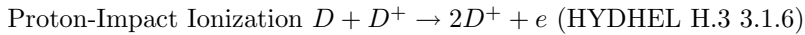
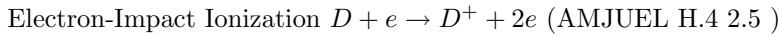
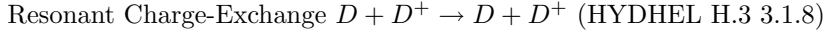
f_{rad} is the fraction of P_{SOL} which is radiated;

T_s^e is the separatrix electron temperature at the outer midplane;

T_s^i is the separatrix ion temperature at the outer midplane;

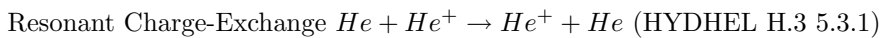
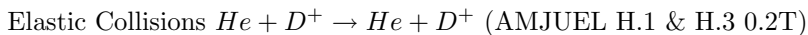
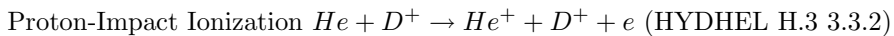
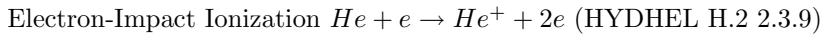
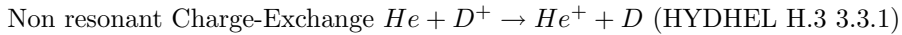
the EIRENE plasma background consists of D^+ , He^{++} and C^{6+} ions. The concentration of the first two is taken from ASTRA results of D^+ , He^{++} and electrons, and the concentration of C^{6+} is then derived to match the electron density. Examples of the SOL radial profiles can be also found in Appendix A, Section 6.4. There also the difference between the old (F12) and new reference (F57) magnetic configurations is discussed.

The Monte Carlo estimates of surface fluxes and spectra relies on a number of basic atomic and molecular processes. Their choice is usually done on a case by case basis. The model applied in the present report for atomic and molecular physics is generally the same as in the regular B2-EIRENE ITER runs, see [6]. Some atomic reactions which might be relevant for the hot plasma have been added. The set of reactions for D atoms is as follows:



Here in parenthesis the corresponding notation in EIRENE databases [7] and [8] is shown. Database HYDHEL is based on the book [9]. Proton-impact ionization could become efficient at \sim keV temperatures and is therefore added to the regular B2-EIRENE reaction set chosen in all recent ITER simulations.

The following reactions are taken into account for He atoms:



The energy spectrum of the incident He atoms could be of critical importance if He-induced blistering [10] takes place. Therefore, in order to get realistic estimate of the amount of energetic He atoms reflected from the hot core plasma, the proton-impact ionization and charge-exchange

are added to the hitherto used reference set of Helium collision processes.

Set of reactions for impurity atoms C and Be:

Electron-Impact Ionization $C + e \rightarrow C^+ + 2e$ (METHANE H.2 2.23)

Electron-Impact Ionization $Be + e \rightarrow Be^+ + 2e$ (AMJUEL H.2 2.4B0)

Charge-Exchange $C + D^+ \rightarrow C^+ + D$ (METHANE H.1 & H.3 3.2)

Elastic Collisions $C + D^+ \rightarrow C + D^+$

Elastic Collisions $Be + D^+ \rightarrow Be + D^+$

The “regular” B2-EIRENE reaction set includes only electron impact ionization. One of the key questions of the present work is to estimate the incident fluxes of impurity atoms to the port-plugs. Neutral impurities can reach them either due to direct line-of-sight transport, or they can be reflected from plasma due to elastic collisions. It is therefore very crucial to include those latter processes in the model. A first series of calculations was performed with C only. Previous studies [3] have shown that calculated C fluxes can provide rough estimates of the Be fluxes as well since Be and C masses, charges and physical sputtering yields are close to each other. An assessment of the sensitivity of the solution to the applied model is shown in Appendix A, Section 6.2.

No atomic data ready for inclusion in the EIRENE simulations on the Be and C elastic collisions with D^+ were available at the beginning of this work. To get the first estimate of the effect of elastic collisions on the incident fluxes the rate of the $He + D^+$ (AMJUEL H.3 0.2T) elastic collisions was used instead, properly scaled with respect to the reduced collision energy. The recent work [11] confirms that the collision rates of $He + H^+$, $Be + H^+$ and $C + H^+$ obtained from quantum-mechanical calculations all have the same order of magnitude and energy dependence. Moreover, for center-of-mass energies larger than 0.1 eV there is a good agreement between quantum-mechanical and semi-classical calculations (the EIRENE database AMJUEL currently provides only semi-classical rates). However, quantitative differences between cross-sections can reach a factor of 5. Therefore, in the future it will be necessary to implement the more accurate fully quantum-mechanically derived collision rates from [11].

To calculate the sputtering yield the EIRENE subroutine SPUTER is applied in the present work. This subroutine is based on the data from the report [12] for normal incidence. The dependence on the incident angle is taken into account according to the “Yamamura fit”, loc cit. and [13]. The carbon chemical sputtering yield is assumed to be 1 % of the incident hydrogenic flux.

3 Technical aspects

One of the main technical challenges for the present project was to develop a flexible way of adding consistently the core plasma region to the simulation domain of the Monte-Carlo code. This problem was addressed in a general way to accommodate also 3D configurations as needed in later project phases. A universal data format was developed to describe EIRENE grids (of different types: 2D, 3D etc.) and a format to describe the transformation of data (mapping) between different grids. These data formats were implemented in the FORTRAN libraries EIRGRID and EIRMAP. Description of the data format and the libraries can be found in Appendix B. This development goes far beyond the scope of the present project and can be used further for grid management and communication between different applications. The original intention was to replace the most frequently used EIRENE triangular grid option by a more general one, in which the grid is defined by polygons with arbitrary number of sides: EIR_TYPE_TORGRID.

The current triangular grid option allows flexible description of any kind of 2D geometry, but it’s disadvantage is that the cells have to be always divided into triangles: e.g. the quadrangular cells of the B2 grid. However, fully removing this inconvenience from the code-procedure proved to be impossible on the time-scale of the project. Therefore a compromise decision was taken to continue to use the triangular grid in EIRENE, but to use the EIRGRID and EIRMAP libraries in the new tools. Triangular grid fits as a special case of the more general EIR_TYPE_TORGRID type.

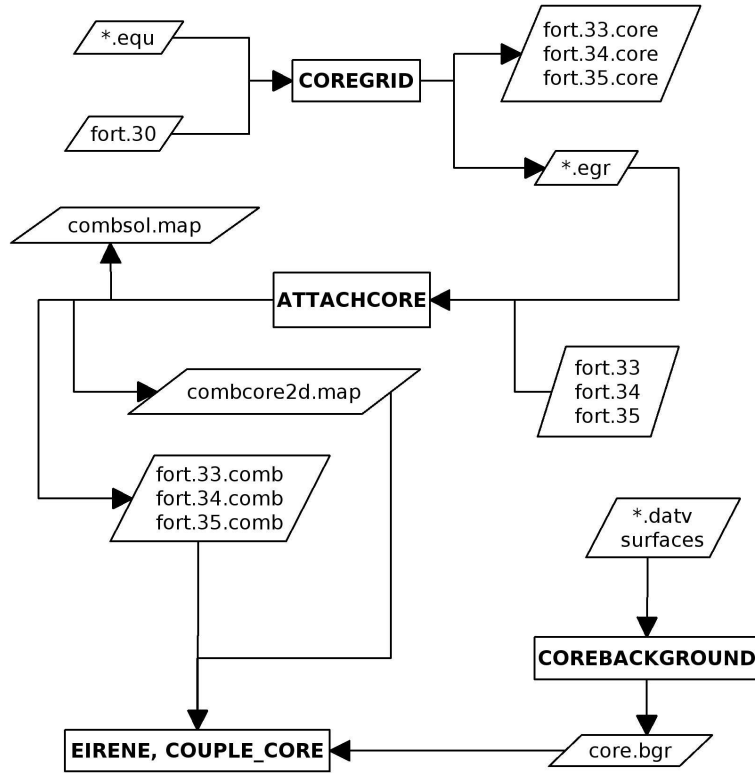


Figure 1: Flow-chart of the core plasma definition for the B2-EIRENE runs

Although a Monte-Carlo code can work on any unstructured grid, the core grid for EIRENE has to be structured in accordance with the magnetic configuration since core plasma parameters are calculated in radial-poloidal coordinates. Usually a 1D “radial” profile is calculated and it is assumed that plasma parameters are constant along the magnetic surfaces. Such a grid: aligned along magnetic surfaces inside the magnetic separatrix, is generated by the grid generator COREGRID written specially for the purpose of this project. This generator consists of the mathematical module CORENODES and interfaces. CORENODES finds magnetic surfaces $\Psi = const$ and calculates positions of the grid nodes on those magnetic surfaces. The magnetic field structure is read from an equilibrium file. The outer boundary of the grid is taken from a file with B2 grid. This allows to adjust the core grid exactly to B2 grid, without any gap. The resulting core grid is stored in the EIRGRID format. A detailed description of COREGRID can be found in Appendix C.

The complete procedure of defining a core grid for the B2-EIRENE run is sketched out in Figure 1. The driver ATTACHCORE combines the grid generated by COREGRID with the triangular grid which was used for the B2-EIRENE run. To do that the standard EIRENE triangular grid is transferred in the EIRGRID format, and the subroutine EIR_GRID_ATTACH of the EIRGRID library is applied. COREGRID can take not only the core-edge interface as the grid boundary, but any “radial B2 grid surface” (surface of constant poloidal flux) which lies inside the magnetic separatrix or the separatrix itself. In this latter case the rings of the B2 grid which overlap with core grid are removed. See for more details in Appendix C. An example of the SOL grid and combined Core-SOL grid is shown in Figure 2.

In EIRENE the plasma parameters on the core grid are specified via interface COUPLE_CORE. This interface reads 0D, 1D or 2D table of the background data and maps them on the combined grid using the mapping (EIRMAP) objects stored in combcore2d.map which is generated by ATTACHCORE. In turn, the table of plasma parameters is produced by MATLAB/Octave scripts which serves as interface to the 1D core calculations. Unfortunately, there is no unified format to represent the result of the core modelling. Therefore, a separate version of the script COREBACKGROUND has to be written for each individual case. An example of the plasma and neutral gas parameters on the full device grid is shown in Figure 3. Technical tests of the new EIRENE option are discussed in Appendix A, Section 6.1.

Spectra of the incident particles are calculated in a steady-state EIRENE run with fixed plasma

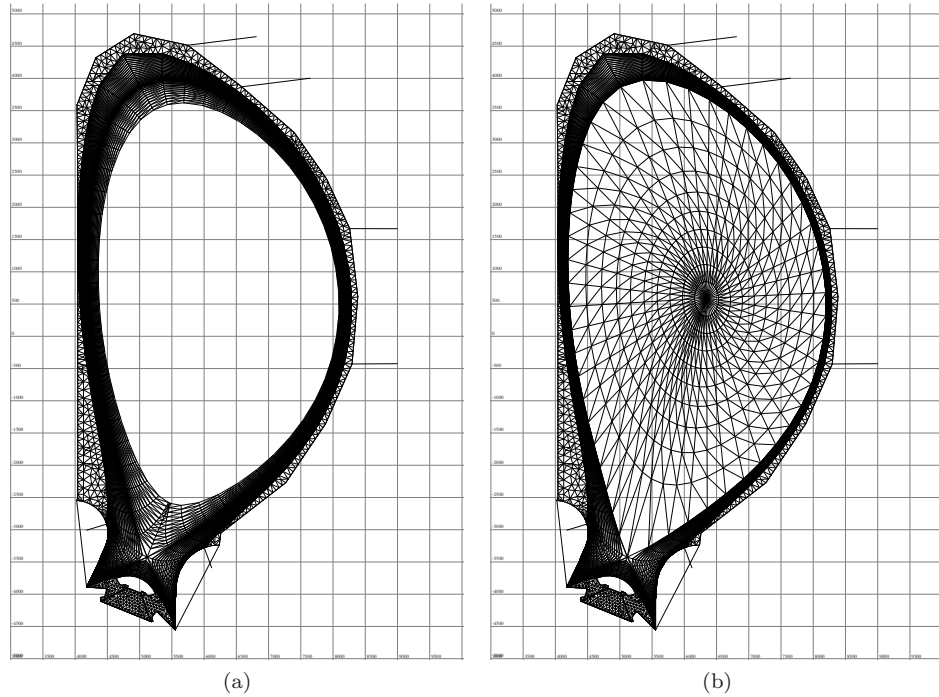


Figure 2: An example of transforming the a) SOL triangular grid into b) combined SOL-Core grid. The core grid is generated by COREGRID and adjusted exactly to the separatrix surface of B2 grid. B2 rings inside separatrix are taken away. Exaggerated core grid (with only a few rings) is shown for the purpose of visualization

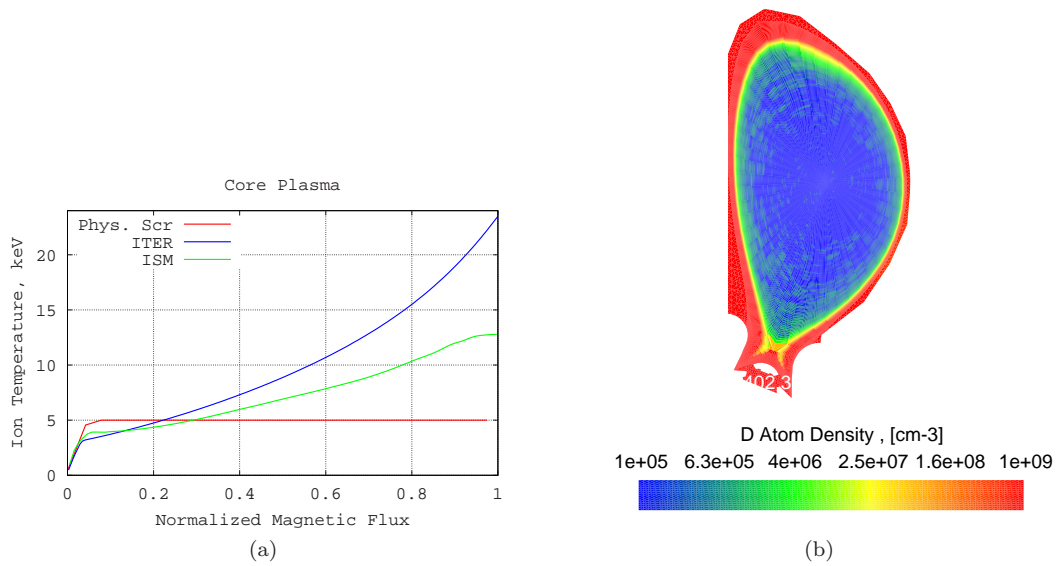


Figure 3: Examples of the 2D distributions plotted on the full device grid (#1542): a) ion temperature; b) D atom density

background. In [5] the line of sight integration was applied to calculate the incident spectrum. This technique allows to obtain very good statistical accuracy. However, this method is physically valid only for charge-exchange collisions of the particles with same mass. For the more general case of elastic collisions, especially between particles of different mass, this method is, strictly speaking, no longer valid. Therefore, in the present work the spectra are calculated directly from the random particle trajectories. Poor statistical accuracy was compensated by application of massively parallel computations carried out on the EFDA fusion supercomputer HPC-FF (hosted by FZ Jülich). The statistical accuracy can still be increased in future by applying the “conditional expectation estimator” of EIRENE, see [www.eirene.de/manual/chapter 1](http://www.eirene.de/manual/chapter%201).

Calculation of spectra in EIRENE is done in the subroutine `CALC_SPECTRUM` and the output is printed by `OUTSPEC`. Control parameters are defined in input Block 10F (loc. cit.). The spectrum is resolved with respect to the incident energy and the (polar) incident angle. In addition to that, sputtering rates of the different materials are calculated directly by so called “user defined surface tallies”. That is, integrals of the sputtering yields over the sampled incident energy and angular spectra: $\int f(E, \theta, \phi) Y(E, \theta) dE d\theta d\phi$, where $f(E, \theta, \phi)$ is the distribution function of the test particles as it appears in the Monte-Carlo run. This integration is implemented in subroutine `UPSUSR`, input in Block 10d. See EIRENE online manual, loc. cit. and more details in Appendix D.

Typical runs were made with $1.067 \cdot 10^9$ test particles: 10^9 particles for the first wall source, $5 \cdot 10^7$ particles for the gas puff, $5 \cdot 10^6$ test particles are used to represent the neutral particle source due to volumetric recombination. The rest of the test particles are used for divertor recycling sources. One stand-alone EIRENE run takes approximately 1 hour of wall-clock time on 256 processors. Some runs were made with 10 times more test particles in order to make sure that the results do not change with better statistics.

4 Preliminary results

4.1 Equatorial Port

Designs of the specific diagnostics have to be prepared for the worst case scenarios. As a criterion for the worst case scenario for sputtering it was decided to take the average kinetic energy of the incident D atoms \bar{E}_D :

$$\bar{E}_D = \frac{Q_D}{\Gamma_D}$$

Here Γ_D is the flux density of the incident D atoms, m^{-2}/s ; Q_D is the heat flux associated with kinetic energy of the incident D atoms, W/m^2 . The poloidal distribution of this parameter along the equatorial port for all studied modelling cases is shown in Figure 5a. “DG surfaces” in this figure are the indexes of the surface elements shown in Figure 4. The equatorial port is comprised of surfaces 15, 16, 17, 18. The “worst case point” is surface 16, #1568, there $\bar{E}_D=560$ eV. Here and below in this Section the term “worst case point” stands for the combination of poloidal position (index of diagnostic surfaces) and the index of B2-EIRENE run. The point surface 16, #1568 also corresponds to the maximum of the effective sputtering yield of Mo: the most probable candidate material for the first mirror, Figure 6a. Here the effective sputtering yield Y_{eff} is defined as:

$$Y_{eff} = \frac{\Gamma_{sput}}{\Gamma_D}$$

Γ_{sput} is the flux of the sputtered material. This is not the point of the maximal Γ_D and, consequently, neither the maximum of Q_D . This latter maximum is reached at surface 18, #1639, Figure 5b.

Surface 18, #1639 is location of the maximal Γ_D in the equatorial port ($1.5e19 \text{ m}^{-2}/\text{s}$), as well as of the maximal sputtering rate for Mo, Figure 6b. However, \bar{E}_D is considered to be a more relevant parameter since the absolute value of Γ_D strongly depends on the model for radial plasma transport which is practically a free modelling parameter. Strictly speaking, Γ_D and \bar{E}_D are not completely independent: poloidal locations with higher Γ_D have lower \bar{E}_D because of the higher far-SOL density. Taking into account the uncertainty in the calculated Γ_D the most plausible conservative estimate is to choose the position of the maximum \bar{E}_D together with maximum Γ_D , despite the fact that this latter is reached in another poloidal segment. Note that surface 16,

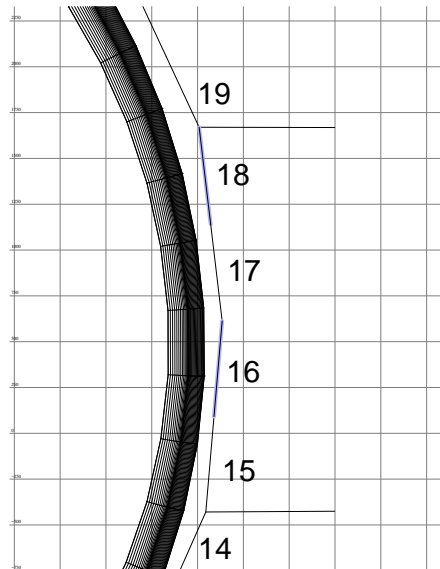


Figure 4: Model of the equatorial port. The numbers correspond to DG surfaces

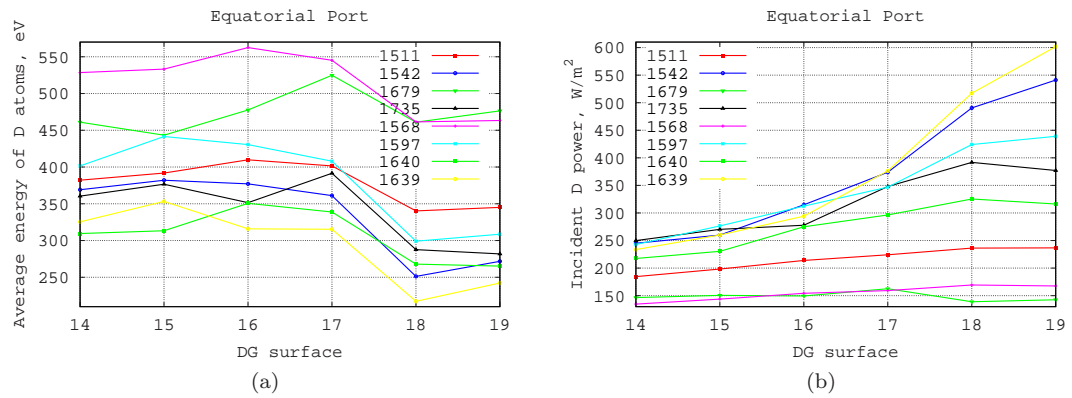


Figure 5: Equatorial Port: a) average incident energy of D atoms; b) total incident kinetic energy of D atoms.

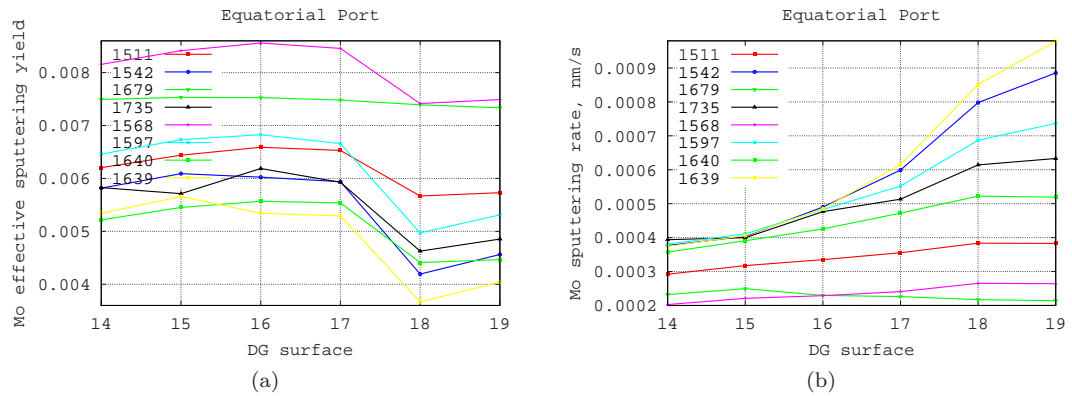


Figure 6: Equatorial Port: a) effective sputtering yield and b) sputtering rate of Mo due to only incident D atoms

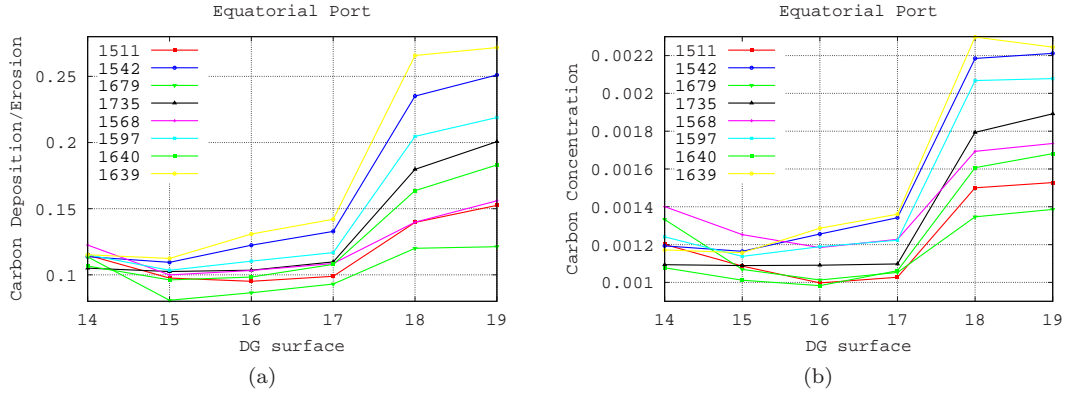


Figure 7: Equatorial Port: a) normalized carbon deposition rate and b) carbon concentration. Here only physical sputtering is taken into account for C and it represents both C and Be

#1568 correspond to the maximum \bar{E}_D and Y_{eff}^{Mo} over the entire first wall (without divertor), not only in the equatorial port.

Net deposition of impurities is in general more difficult to estimate than erosion of the mirror material. Port plugs will be installed in the magnetic shadow of the blanket modules. Therefore, it can be assumed here that no ions but only neutral particles can reach the port-plug entrance. A first crude estimate of the deposition is made for the first wall (without taking into account the diagnostic duct). As a figure of merit to find the worst case the following ratio (normalized deposition) is used:

$$R = \frac{\Gamma^{imp}}{\Gamma_{imp}^{sput}}$$

Here Γ^{imp} is the incident flux of impurity atoms and Γ_{sput}^{imp} is the flux of impurity bulk material sputtered by the incident D atoms. In the current calculations only Carbon impurities are considered. From the previous experience [3] it is known that calculated C and Be concentrations are fairly close to each other (because of their similar physical properties). If only physical sputtering is taken into account, then the results obtained for C can serve as an estimate of the normalized Be deposition as well. A ratio $R < 1$ corresponds to net deposition. Larger R values mean a smaller margin between erosion and deposition. The largest R is reached at Surface 18, #1639. Even in this worst case erosion is almost a factor of 4 larger than deposition. Therefore, net erosion conditions can be expected in the whole equatorial port. The largest C concentration: 0.0025, is reached in the same position. The relative impurity concentration in the incident flux is defined here as:

$$C_{imp} = \frac{\Gamma^{imp}}{\Gamma_D}$$

4.2 Upper Port

The same criteria as for the equatorial port are applied to identify the worst case at the upper port. Conditions in the upper port are very different with and without gas puff, Figure 9a. In this plot the upper port is composed of surfaces 25, 26, 27, 28 shown in Figure 8. Without gas puff the incident kinetic energy of the D atoms \bar{E}_D is almost as high as at the equatorial port. When the gas puff is switched on the plasma in front of the upper port gets colder and more dense, see Figures 23b, 23d and 23f in Appendix A, Section 6.4. As a result \bar{E}_D is drastically reduced. But the incident flux of D atoms Γ_D is significantly increased due to particles originated from gas puff, Figure 9b. Maximum Γ_D reaches $3e21 \text{ m}^{-2}/\text{s}$ (Surface 26, #1639). Note that all calculations are made on assumption of a *toroidally uniform* gas puff.

Two cases are therefore considered. The first case is the upper port without gas puff there one can assume the same “worst case” in the equatorial port. To assume the same energy distribution with gas puff but increased Γ_D would lead to a significant overestimation of sputtering. Therefore, as criterion for the worst case the kinetic energy flux of the incident D atoms Q_D (the product of \bar{E}_D and Γ_D) is taken. The maximum of this flux is reached on the Surface 25, #1639, Figure 9b. This worst case point corresponds to the maximum of the erosion rate of Mo as well, Figure 10b.

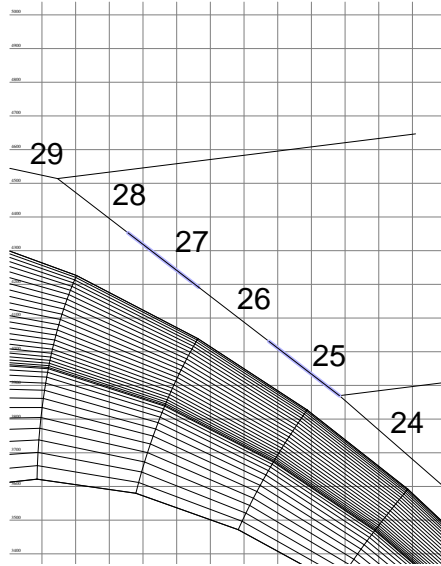


Figure 8: Model of the upper port. The numbers correspond to DG surfaces

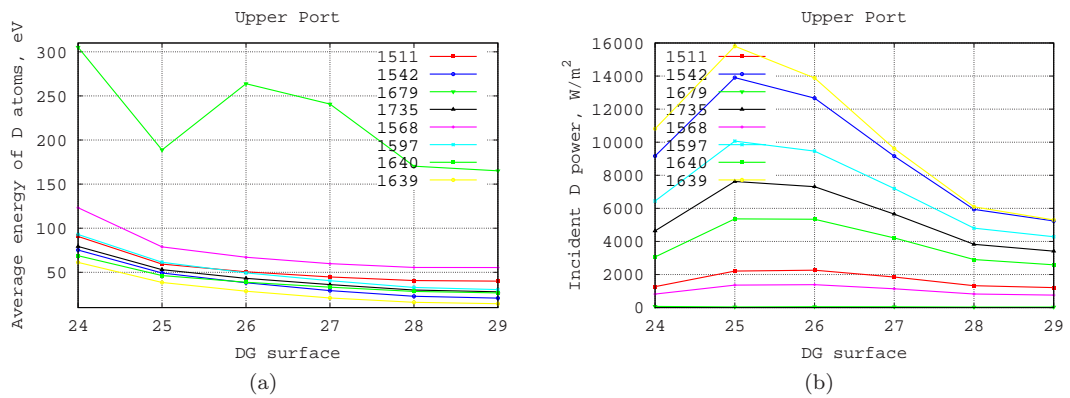


Figure 9: Upper Port: a) average incident energy of D atoms; b) incident kinetic energy of D atoms.

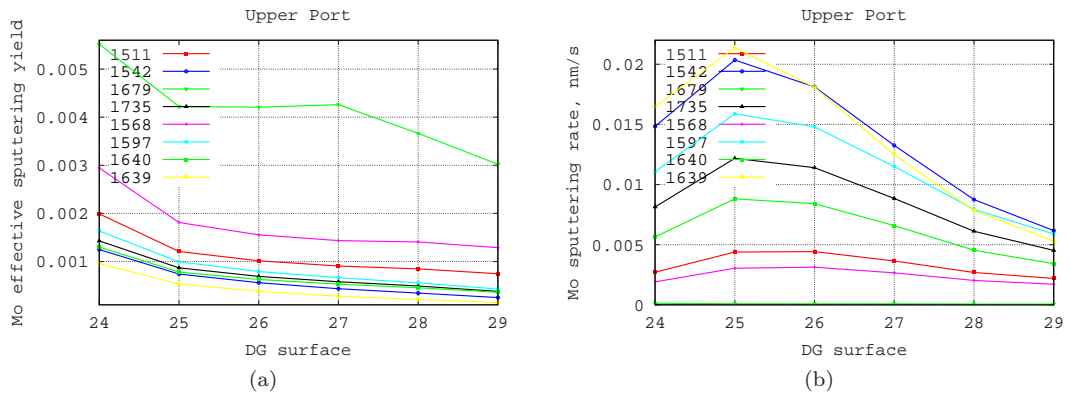


Figure 10: Upper Port: a) effective sputtering yield and b) sputtering rate of Mo due to only incident D atoms. Here only physical sputtering is taken into account for C and it represents both C and Be

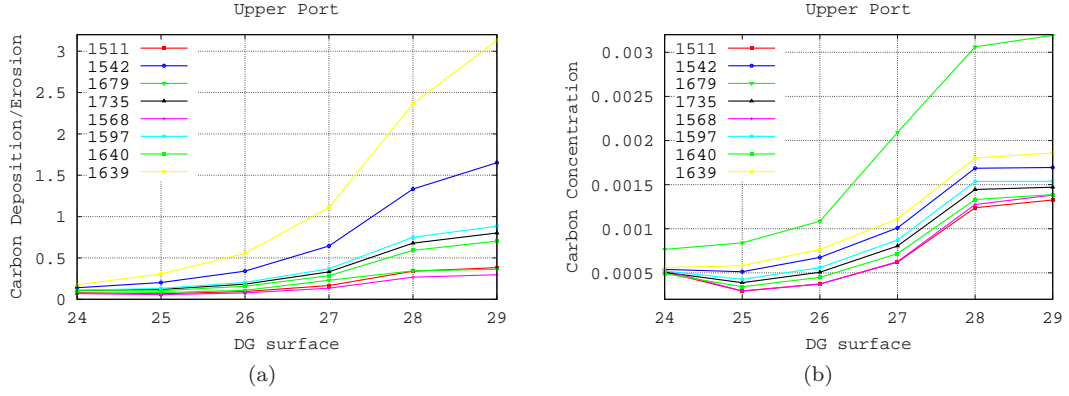


Figure 11: Upper Port: a) normalized carbon deposition rate and b) carbon concentration

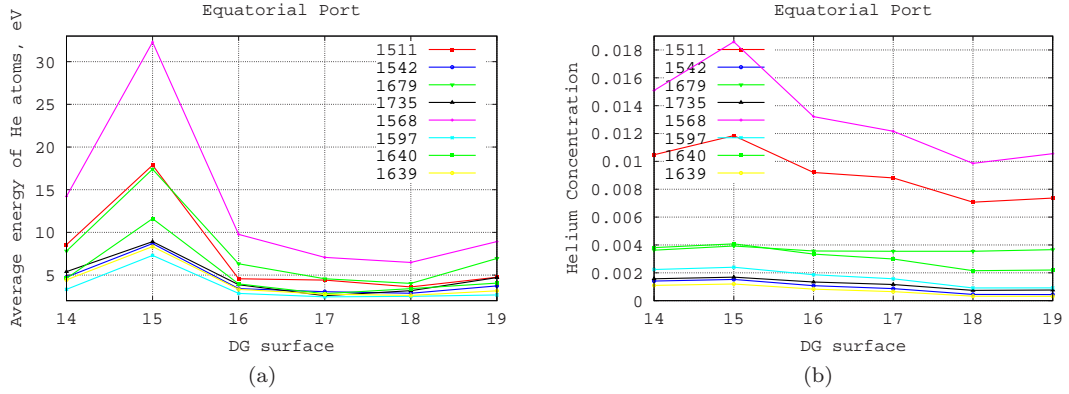


Figure 12: Equatorial Port: a) average incident energy of the He atoms b) He concentration in the incident flux

The normalized carbon deposition rate R (defined in the previous section), Figure 11a, experience a large poloidal variation along the port surface, with values differing by more than an order of magnitude. This result makes it difficult to propose a worst case which would be relevant for the whole port. In the upper part of the port (surface 28) the calculated R exceed 1, indicating net deposition there. In some parts of the port erosion is larger than deposition. However, the same large margin as in the equatorial port in which erosion is 4 times larger than deposition), can be reached only in the lowest part of the port (surface 25). Therefore, the simulation results do not guarantee net deposition conditions in the whole upper port.

4.3 Helium

Helium atoms could in principle lead to much more efficient sputtering than DT atoms due to their larger mass. Calculations made with “handbook” values of the sputtering yield show that sputtering due to He is negligible compared to that due to main ions. There are, however, experimental indications that the erosion can be significantly enhanced due to He induced blistering [10]. In order to estimate this effect the fluxes and incident energies of the He atoms have to be known.

Same as for D atoms, the criterion for the “worst case” energy distribution of the incident He is the average incident kinetic energy \bar{E}_{He} . The maximum of this energy (maximum over the whole first wall without divertor) is reached at the equatorial port, surface 15, #1568, see Figure 12a. This point the maximal He concentration (0.02) as well, Figure 12b. Here “He concentration in the incident flux” is the ratio of the incident flux of He atoms to that of D atoms.

4.4 Divertor

Several diagnostic surfaces were located beneath the dome structure, in the middle. This is the location of periscopes. Fast particles practically do not reach this surface, neutral particles are thermalized and their energy distributions are almost Maxwellian. An example is shown in

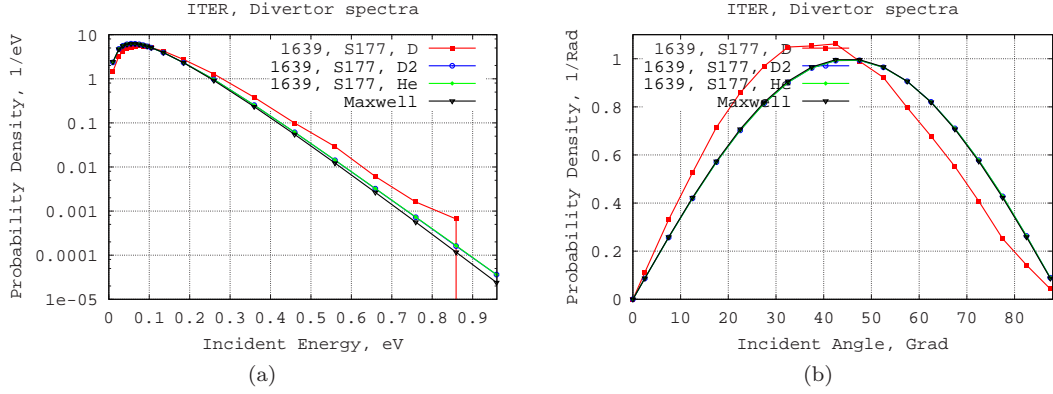


Figure 13: Divertor sub-dome: a) energy and b) angular distribution on the diagnostic surface beneath the dome (in the center) for the high density case #1639

Figure 13 for the highest density case #1639. In Figure 13a the energy distributions computed by EIRENE are compared with the incident energy spectrum of a Maxwellian gas (see Section 9.3):

$$f(E) = \frac{E}{T^2} \exp\left(-\frac{E}{T}\right) \quad (1)$$

The temperature T was chosen as a half of the average kinetic energy of the incident He or D₂ (the average energy of the distribution function (1) is $2T$). The value of this temperature 0.059 eV is only slightly higher than that of the dome walls: 0.05 eV. The distribution functions of He and D₂ are very close to each other and both are close to a Maxwellian distribution. Deviations are seen only in the high energy tail. There is also a small amount of high energetic particles with $E > 1$ eV coming directly from the hot plasma. The distribution function of D atoms deviate stronger from a Maxwellian. This is explained by the fact that in the applied model D atoms of low energies can leave the surface only as D₂ molecules. Therefore, the atoms incident to the diagnostic surface come directly from plasma and can be cooled down only by neutral-neutral collisions. A similar picture is seen for the incident angle, Figure 13b. Here “incident angle” θ is the angle between the outer normal of the surface element and the velocity of the incident particle. The thermal gas distribution in Figure 13b is described by the formula $2 \sin \theta \cos \theta$.

In the cases with lower density the amount of high energetic particles is larger, but the calculated erosion rates are still extremely low. For example, the maximum erosion rate of Mo due to incident D atoms is $3 \cdot 10^{-5}$ nm/s (#1568). Incident carbon fluxes are always at least 3 orders of magnitude (!) larger than the sputtered fluxes. Maximum carbon concentration: the ratio of the incident carbon flux to the incident D atom flux, is 5 %. Therefore, deposition dominated conditions are to be expected at this location for both C and Be, unless C chemical sputtering yield is not larger than 5 %. The maximum calculated C incident flux is $5e19$ m⁻²/s, that is 0.4 nm/s.

The incident flux of D₂ molecules varies from $6e22$ to $6e23$ m⁻²/s, depending on the divertor density. For thermal particles with temperature 0.05 eV this flux corresponds to the density from $1.4e20$ to $1.4e21$ m⁻² or to the pressure from 1.1 to 11 Pa.

No analysis have been made for the gap between divertor cassettes so far. Such an analysis will require detailed knowledge of the divertor and port design.

4.5 Summary

Preliminary analysis of the 8 B2-EIRENE simulations indicated “worst case points” from the point of view of sputtering and net impurity deposition. Here “point” stands for the combination of poloidal position (index of diagnostic surfaces) and the index of B2-EIRENE run. Worst case for sputtering in the equatorial port (and in the whole vacuum vessel without divertor) is surface 16, #1568. Worst case for the net impurity deposition is surface 18, #1639. The maximum carbon concentration in the incident flux is 0.0025. Even in this case the calculated erosion rate of C (due to only physical sputtering) is a factor of 4 larger than its deposition rate. A similar result is expected for Be. Thus, net erosion conditions in the whole equatorial port are to be expected.

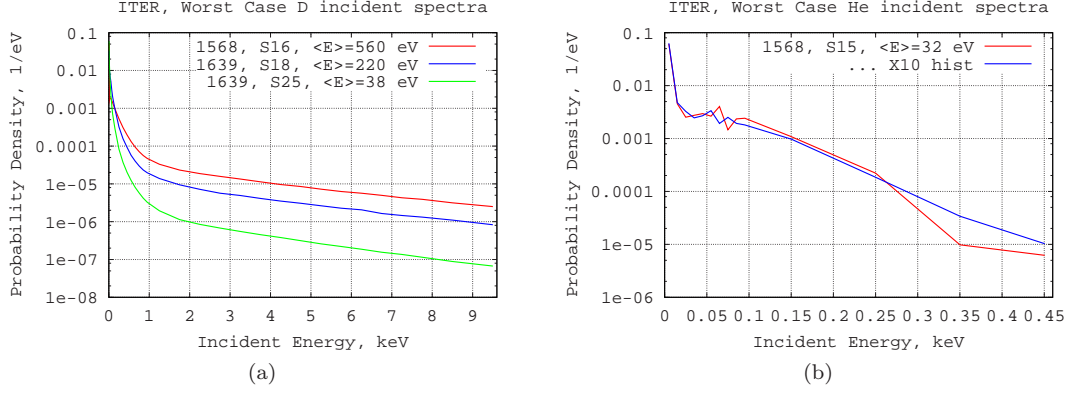


Figure 14: “Worst case” incident energy spectra of a) D and b) He atoms

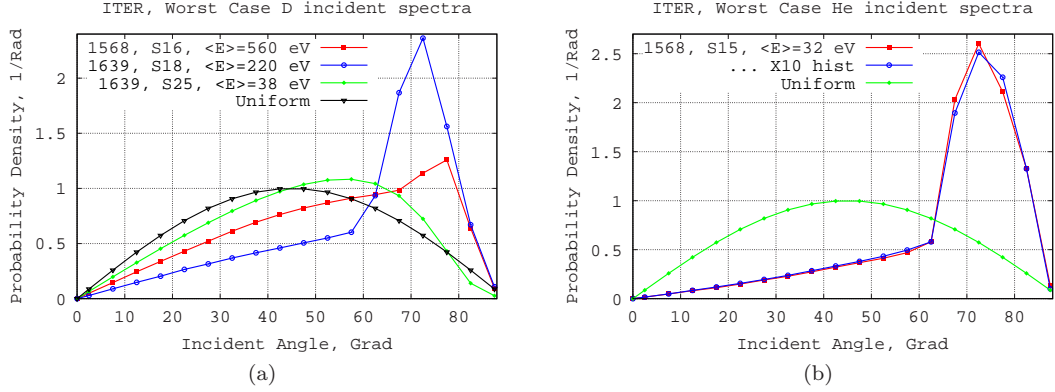


Figure 15: “Worst case” distribution functions of the incident angle of a) D and b) He atoms. “Incident angle” θ is the angle between the surface outer normal and incident velocity: 0 correspond to normal incidence. “Uniform” stand for the case with uniform distribution of the incident flux over all directions ($2 \sin \theta \cos \theta$)

The calculated maximal incident flux of D atoms Γ_D is $1.5e19 \text{ m}^{-2}/\text{s}$. In the B2-EIRENE simulations processed in this report purely diffusive cross-field transport was assumed with an effective “diffusion-” velocity at the far-SOL boundary of only 10 m/s. Experiments in the existing tokamaks show that a strong convective transport exist with effective radial velocity up to 100 m/s [14]. Therefore, the incident flux calculated by B2-EIRENE could be significantly underestimated. To take into account this uncertainty it is suggested here to increase the calculated Γ_D by a factor of 10. After rounding off this yields $\Gamma_D=2e20 \text{ m}^{-2}/\text{s}$.

Conditions in the upper port without gas puff are almost the same as in the equatorial port. With gas puff the worst case for the sputtering is Surface 25, #1639. In this case the peak Γ_D reaches $3e21 \text{ m}^{-2}/\text{s}$ (on assumption of toroidally uniform gas puff). The normalized C deposition rate changes by an order of magnitude along the port surface. At some locations net deposition is indicated. Therefore, no guarantee of the net erosion conditions in the upper port can be given.

Worst case for the sputtering due to He atoms (over the whole main chamber without divertor) is found for the surface 15, #1568. Criterion for this worst case is the highest average kinetic energy of the incident atoms.

Energy and angular distributions of the incident D and He atoms for the worst cases listed above are shown in Figures 14 and 15. Angular distributions have maximum at grazing incident angles because of longer lines of sight which collect more particles from the “collision source” of finite size.

In divertor only the periscope location beneath the dome structure has been analyzed. High energetic particles practically do not reach this area. As a result, the sputtering is extremely low, e.g. the maximal calculated sputtering rate of Mo is $3 \cdot 10^{-5} \text{ nm/s}$ (#1568). Deposition dominated conditions are expected for both C (chemical sputtering possible) and Be (only physical sputtering). The maximum calculated carbon deposition rate there reaches 0.4 nm/s (#1679).

5 Outstanding issues and plans

Calculating the incident impurity fluxes is one of the main tasks of the present project. Elastic collisions with main ions can substantially increase those fluxes. It is therefore mandatory to use the most up to date model for the impurity elastic collisions published recently in [11]. These data have kindly been made available by the authors in the on-line database www-cfadc.phy.ornl.gov, after request from this present project. These new collision rates will have to be implemented in the present EIRENE model as soon as possible. Be has to be added and Be-covered wall has to be considered as being more realistic than a C-coated wall. The sputtering yields of D and T are different and their incident spectrum can be different as well. It is therefore desirable to split the current model isotope D into D and T.

Statistical accuracy of the spectrum calculations can be further increased by applying the “conditional expectation estimator” option of EIRENE. Calculation of the statistical variations have to be tested and applied as a standard error bar diagnostic.

Analysis of the conditions in the divertor cassette seems to be more difficult than in the main chamber because of the very non-uniform plasma and gas parameters and the complex geometry there. It could be the case that 2 dimensional calculations made for the plasma facing surfaces bring no useful information at all and the detailed 3D divertor and port-plug design have to be taken into account. The EIRENE code is capable to deal with such fully 3D configurations, although setting up geometric input is somewhat demanding (as for any 3D Monte Carlo code). Preliminary discussion with representatives of the ITER team might be necessary. 3D effects are also possible in the upper port if the gas puff is not toroidally uniform. In this case it is necessary to know the exact location and design of the gas puffing slots.

Reference ITER calculations studied in this report were made on assumption of purely diffusive radial transport. Strong radial convection in the far-SOL (as observed in experiments) can significantly increase incident fluxes on the first wall. At the same time, for the old magnetic configuration F12 it was shown that radial convection does not lead to significant modification of the density profiles. Such test can be repeated for the new configuration as well, although this lies outside of the scope of the present project.

References

- [1] Kukushkin A S, Pacher H D *et al.* 2009 *Nuclear Fusion* **47** 075008
- [2] Kukushkin A S, Pacher H D *et al.* 2005 *J. Nuclear Mater* **337-339** 50
- [3] Kotov V *et al.* 2009 *J. Nuclear Mater* **390-391** 528
- [4] Reiter D, Baelmans M and Börner P *Fus. Sc. Tech* **47**, 172 (2005) and www.eirene.de
- [5] Verbeek H *et al.* 1998 *Nuclear Fusion* **38** 1789
- [6] Kotov V, Reiter D and Kukushkin A S 2007 *Numerical study of the ITER divertor plasma with B2-EIRENE code package* Report Jül-4257, www.eirene.de/kotov_solps42_report.pdf
- [7] Reiter D *et al.* *Database AMJUEL* www.eirene.demanuals/amjuel.pdf
- [8] Reiter D *et al.* *Database HYDHEL* www.eirene.demanuals/hydhel.pdf
- [9] Janev R K, Langer W D, Evans K and Post D E 1987 *Elementary processes in hydrogen-helium plasmas* (Springer)
- [10] Yoshida N *et al.* 2005 *J. Nuclear Mater* **337-339** 942
- [11] Krstic P S and Schultz D R 2009 *Phys. Plasm.* **16** 053503
- [12] Eckstein W, Bohdansky J, Roth J and Ottenberger W 1993 IPP 9/82 Max Plank Institute für Plasma Physik
- [13] Yamamura Y and Shindo S 1984 *Radiation Effects and Defects in Solids* **80** 57
- [14] Lipschultz B *et al.* 2005 *Plasma Phys. Control. Fusion* **47** 1559
- [15] Kotov V *et al.* 2009 *Phys. Scr. T* **138** 014020

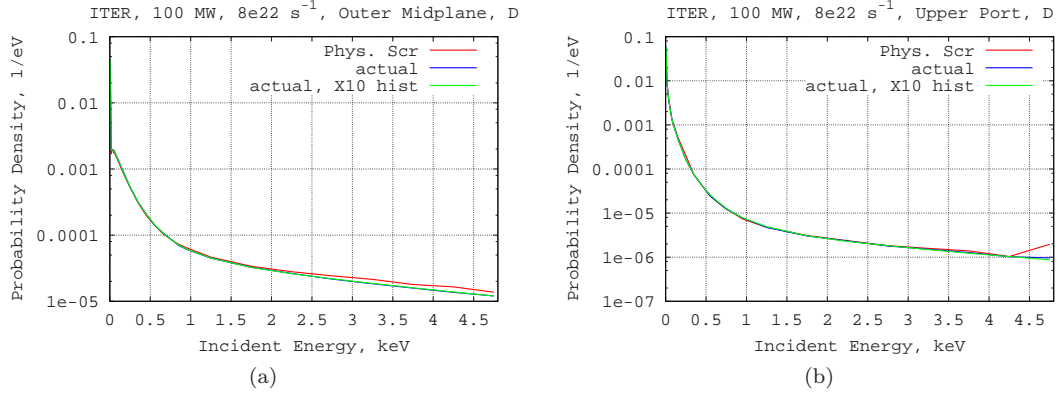


Figure 16: Comparison of the incident energy spectra of D calculated with the old (“Phys. Scr”) and new (“actual”) option at the a) outer midplane and b) upper port. Green curve shows calculations made with 10 times more histories in order to estimate the statistical error.

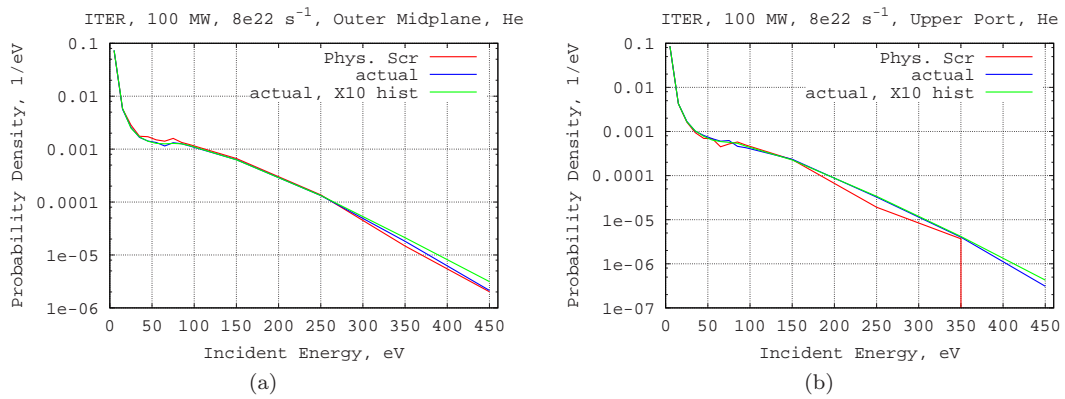


Figure 17: Comparison of the incident energy spectra of He calculated with the old (“Phys. Scr”) and new (“actual”) option at the a) outer midplane and b) upper port. Green curve shows calculations made with 10 times more histories in order to estimate the statistical error

6 Appendix A: Sensitivity assessment

6.1 Verification

Prior to any further investigation it had to be verified that EIRENE works properly on the converted combined grid and the core plasma background is correctly specified. A necessary condition which has to be fulfilled is that there are no error messages from any of EIRENE routines. The code compiled with array bounds check with both Portland Group and INTEL compilers did not detect any mistake as well. A no-harm test was passed: with closed core-edge interface the code produces exactly the same result on the combined grid as before. 2D profiles of the core and SOL plasma were plotted and it was checked visually that the specification is correct. Some examples are shown in Figure 3.

Finally, incident particle spectra which were calculated previously in [15] were reproduced. In [15] a much more primitive option was used, assuming constant plasma parameters in the whole core zone (one core cell). The results of the comparison are shown in Figures 16 and 17. For D spectra the relative difference is always below 20 %, except the feature at the high energy tail in the old calculations, Figure 16b. Calculation of statistical variation for the spectrum was not yet tested for this study. Therefore, in order to estimate statistical error one more calculation was made with 10 times more histories: green curve in Figures 16 and 17. This test shows that the discrepancy is systematic and is not related to statistical variation.

For the He spectra at the outer midplane the statistical variation is small up to 250 eV. In this energy range the relative difference is within 20 %, as for D. At the outer midplane the discrepancy is much larger, even for energies below 350 eV: the domain of low statistical variation.

Currently the test results are considered to be satisfactory. The reason for the systematic

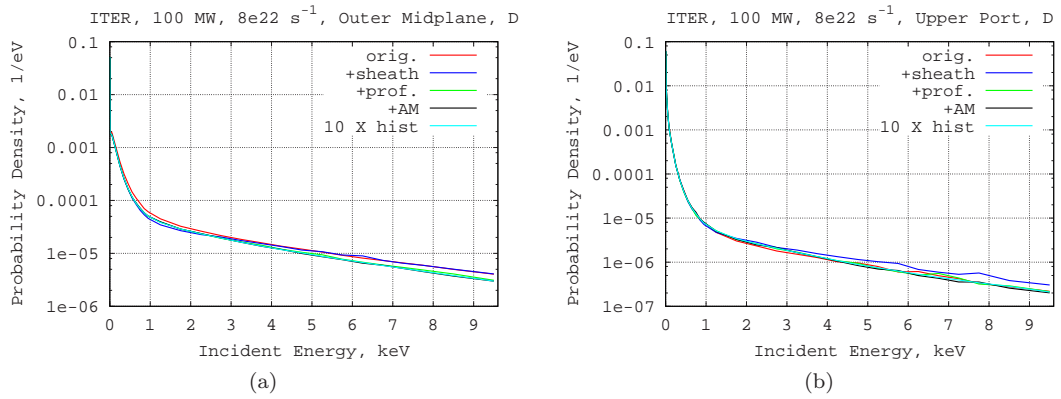


Figure 18: Comparing incident energy spectra of D at a) equatorial port and b) upper port for the different model assumptions. The legend is described in Section 6.2

discrepancies has to be investigated in the future. The main reason could be that the plasma parameters used in old calculations were not completely matched. The test calculations were made with core grid completely replacing the B2 core rings. However, distinct from the B2 grid the COREGRID-generated grid is not orthogonal, and in the considered case small poloidal variation of plasma parameters persisted in the core. Besides that, in the old runs several steps of B2-EIRENE but not the EIRENE stand-alone runs were made. It was found that by coincidence the plasma parameters used on the last B2 time-step were not saved and they slightly differ from those at the beginning (saved in `fort.30`).

For each EIRENE stand-alone diagnostic run the parameters of the neutral gas (from `fort.44`) were plotted and compared to those from the original B2-EIRENE run. This is done to make sure that there are no significant changes, as expected, and that the parameters of the stand-alone run exactly match those of the coupled run.

6.2 Sensitivity with respect to the applied model

The model which was applied in [15] was updated stepwise to follow the effect of each individual step. The results are shown in Figures 18 and 19. Red curves in the figures correspond to the calculations shown in the previous section. Normally sheath acceleration is not taken into account in the B2-EIRENE calculations for the incident ions at the “parallel” walls: option `NEMOD=6`. This is not completely correct but could help to avoid significant overestimate due to overestimated wall temperature. For the diagnostic runs the sheath acceleration was switched on: blue curve. The primitive radial profile with uniform core plasma was replaced by a more advanced one, obtained from 1D transport simulations made in frame of the Integrated Tokamak Modelling EFDA task force, see next section. The result is shown by the green curve. Finally, atomic physics was updated to that discussed in Section 2: black curves. As in the previous section, a run with 10 times more histories was made at the end to estimate the statistical error: cyan curves.

The D spectrum is not sensitive to the modifications of the model, Figure 18. Maximum difference (maximum over all energy bins) at the outer midplane is within 30 %. However, replacing the core profile produces a visible change in the high energy part of the spectrum. The difference due to sheath acceleration is surprisingly large: up to 70 % at the upper port. However, other modifications reduce the difference there down to 20 %: similar figure as at the equatorial port.

He energy spectra are much more sensitive to the model modifications, Figure 19. In particular, to the updated atomic physics. This is not surprising since the reaction set used in the diagnostic runs has charge-exchange collisions. They lead to increased amount of atoms reflected from the hot regions seen in the high energetic tail of the distribution function.

6.3 Sensitivity with respect to the core plasma profiles

Several shapes of the core plasma profile were investigated. They are shown in Figure 20. Red curves are the simplified profiles used in [15]. Green curves show the profile calculated in frame

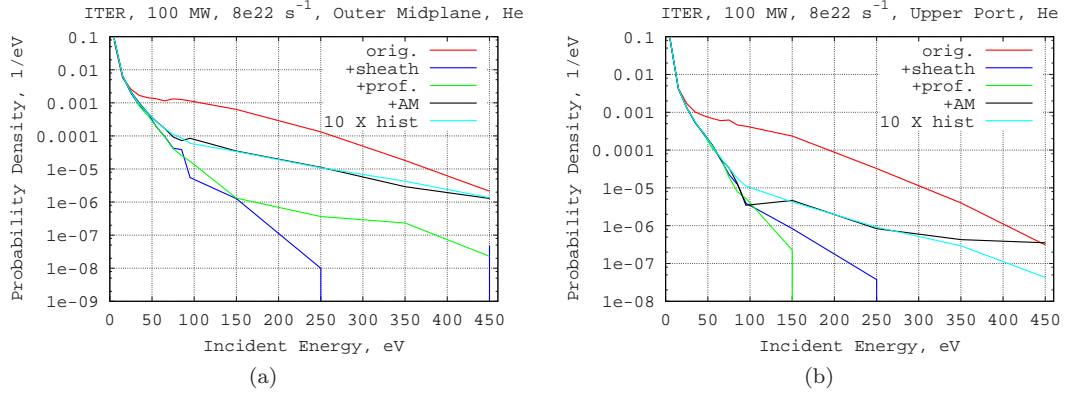


Figure 19: Comparing incident energy spectra of He at a) equatorial port and b) upper port for the different model assumptions. The legend is described in Section 6.2

of the ITER Modelling Group of the European Task Force “Integrated Tokamak Modelling” (ISM). The simulations were made for a pellet fueled plasma, therefore the density profile is peaked. When transforming the core profiles for EIRENE it was assumed that the difference between electron and main ion density is build up by He^{++} ions. Blue curves correspond to the ITER simulations made with the ASTRA code by the ITER Team taken from the document [Yu. Gribov, T. Casper, A. Polevoi, ITER IDM ITER_D.2V2XYR]. It was assumed that the EIRENE plasma background consists of D^+ , He^{++} and C^{6+} ions. The concentration of the first two was taken from the ASTRA results, and the concentration of C^{6+} was taken to match the electron density.

Spectra of the incident atoms calculated for the different core profiles are shown in Figures 21 and 22. The ITM profile leads to a slightly larger amount of high energetic particles than the ITER profile. This is a consequence of the larger temperature at the edge, see Figures 20a and 20b. At the equatorial port the difference in $f(E)$ reaches 35 % at the 10 keV energy, at the upper port: 50 %. The effect on the high energetic part of the He spectrum is smaller than that for D.

The core plasma profile of the ITER Team is used in all simulations shown in the rest of this report.

6.4 The effect of magnetic configuration

In 2009 the shape of the ITER divertor was changed as well as the magnetic configuration. In the new configuration F57 the SOL is approximately twice as broad as in the old one. The distance between the outer edge of B2 grid and the wall (clearance) is reduced. Radial profiles of the plasma parameters calculated with old and new magnetic equilibrium are shown in Figure 23. Both cases shown had input SOL power 100 MW and similar gas puffing rates: $17\text{e}22 \text{ s}^{-1}$ for F12 configuration (#1055p3) and $15.5\text{e}22 \text{ s}^{-1}$ for F57 (#1542) configuration. The solutions could not, of course, be completely matched. In particular, the separatrix density is always higher with the F57 configuration. Broader scrape-off-layer leads to lower temperature and density at the edge of the grid because of more space for radial decay. At the same time, in the far-SOL the profiles are almost flat. This indicates that in simulations made for F57 the plasma parameters at the edge of B2 grid yield much more realistic estimates of the parameters at the wall than those obtained in F12. This is the case especially in front of the gas puff, see e.g. Figure 23b.

Consequences of the modifications of the radial profiles are clearly seen on the incident energy spectra, Figures 24 and 25. The results for two different divertor densities are shown for F57 configuration: low density (#1511) and high density (#1542). The modelling case for F12 configuration (1055p6.be.cv2) does not exactly match either of those densities, but the trend is clearly seen. The amount of high energetic ($E > 1 \text{ keV}$) D atoms obtained with F12 is almost twice as large as that obtained with F57 at both upper and equatorial ports: less particles can reach the region of hot plasma with the broader SOL. Consequently, the average energy of the incident D atoms is reduced from 810 eV to 350-410 eV, and e.g. the effective sputtering yield of tungsten is reduced from $5.5 \cdot 10^{-3}$ to $(2.6 \dots 2.9) \cdot 10^{-3}$. A qualitatively similar effect: reduced amount of high energetic atoms, is seen for the He spectra as well. However, in this case the effect almost

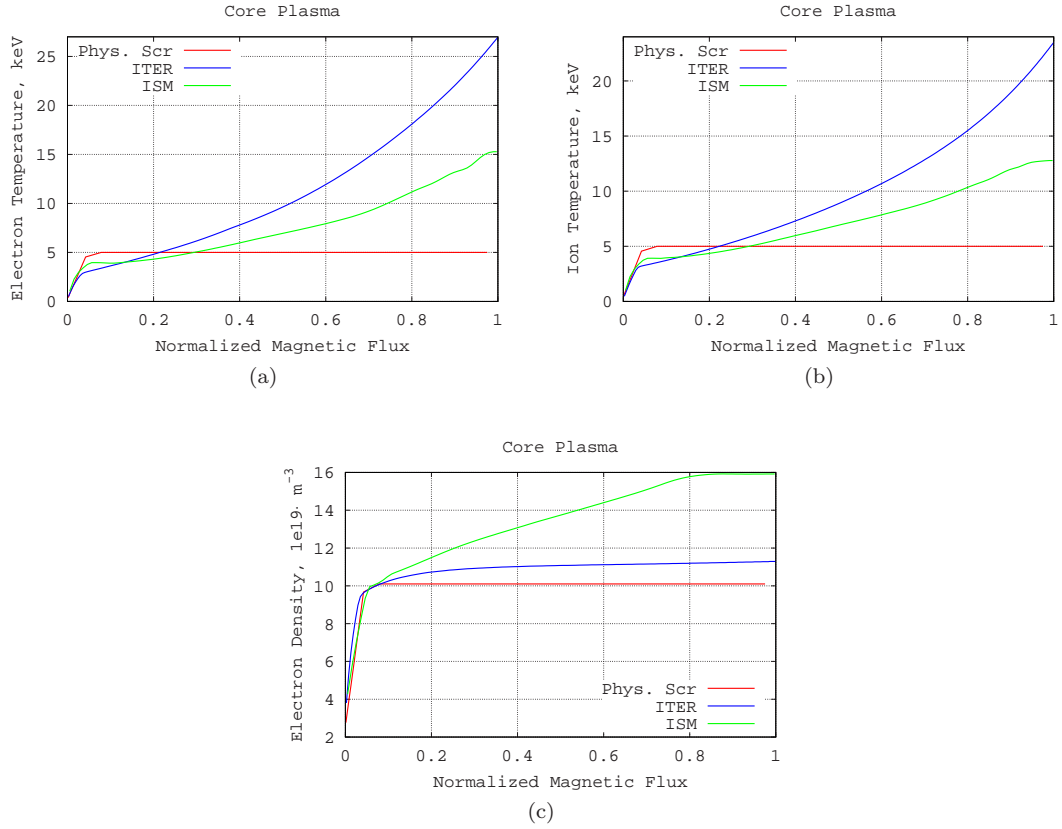


Figure 20: Radial profiles of the core plasma parameters used in the simulations. The legend is described in Section 6.3

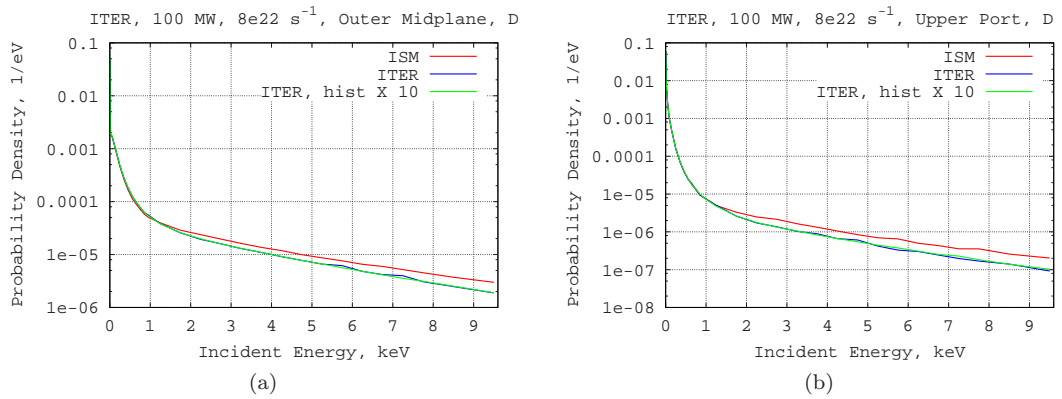


Figure 21: Comparing incident energy spectra of D at a) equatorial port and b) upper port for the different core plasma profiles

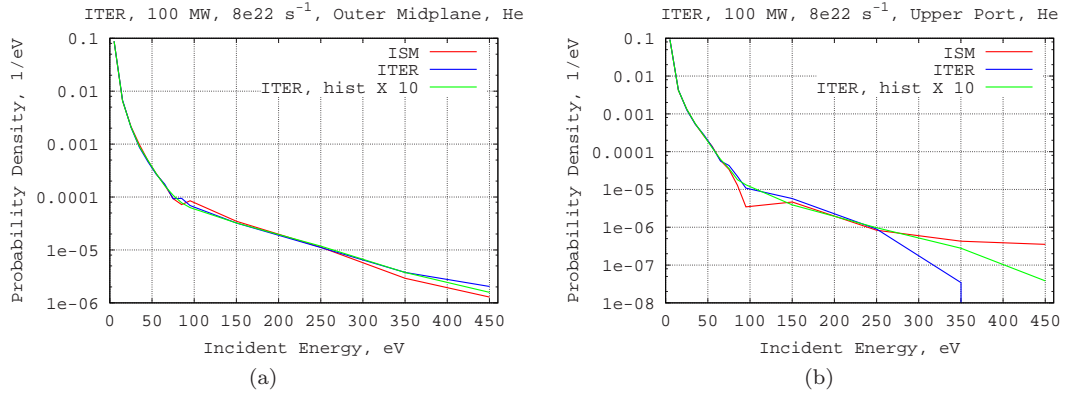


Figure 22: Comparing incident energy spectra of D at a) equatorial port and b) upper port for the different core plasma profiles

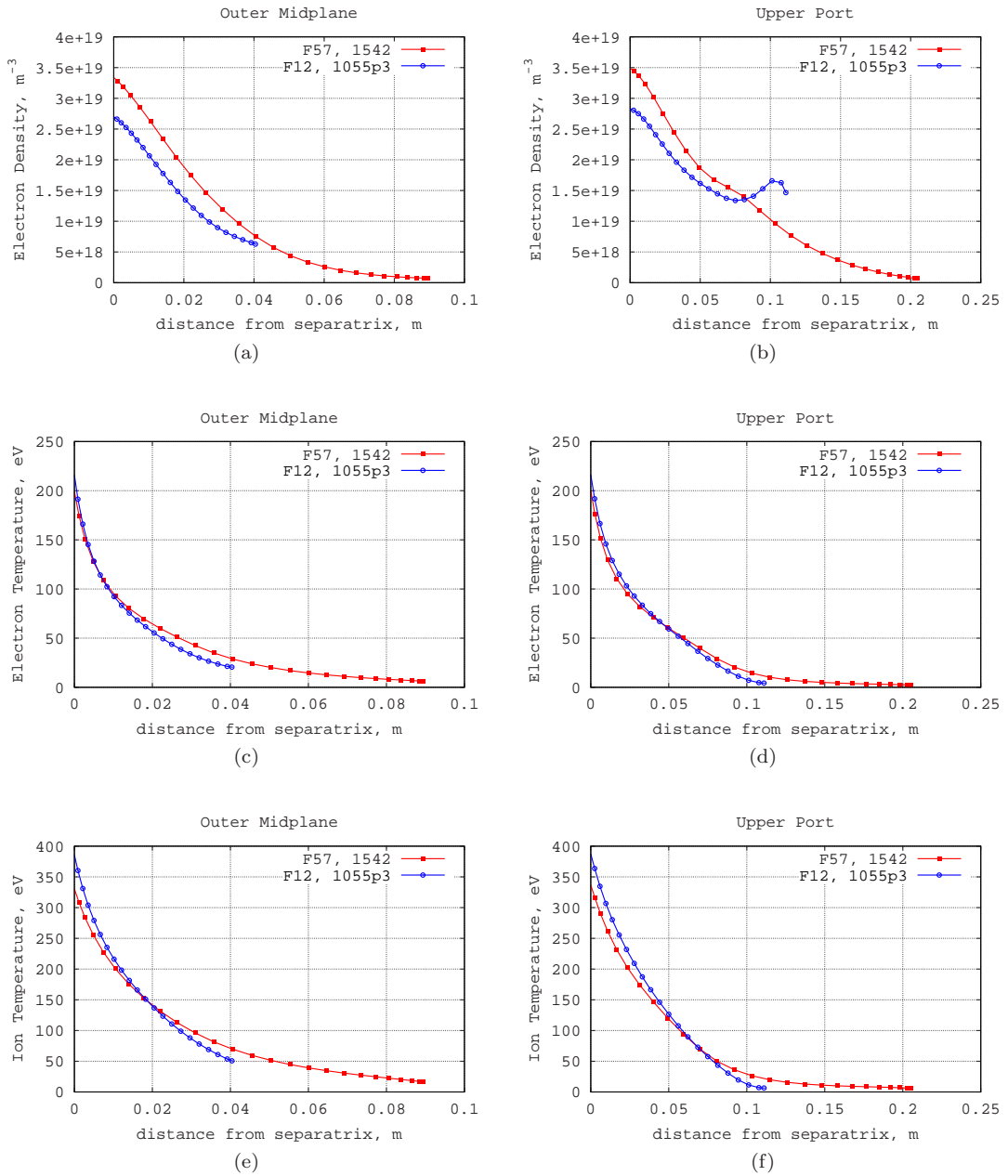


Figure 23: Radial plasma profiles in front of a) the equatorial and b) upper ports for the old (F12) and new reference (F57) ITER magnetic configuration. The gas puff is located in the upper port.

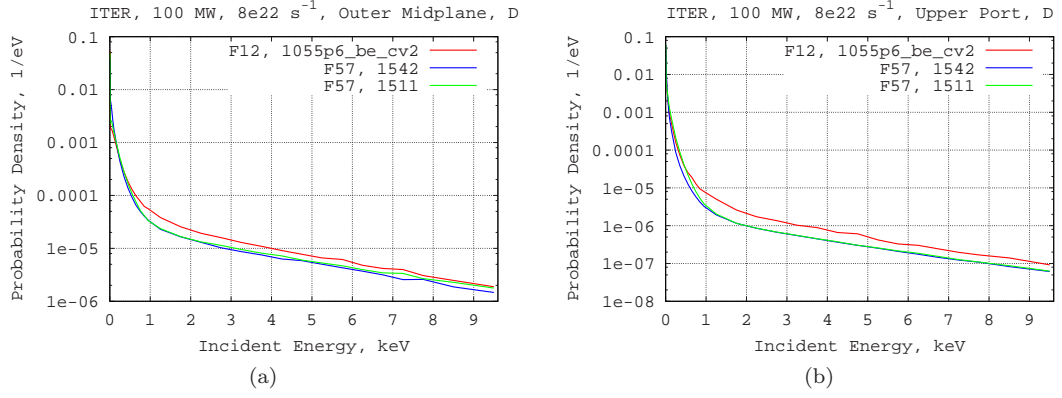


Figure 24: Comparing incident energy spectra of D at a) equatorial port and b) upper port for old (F12) and new reference (F57) ITER magnetic configuration

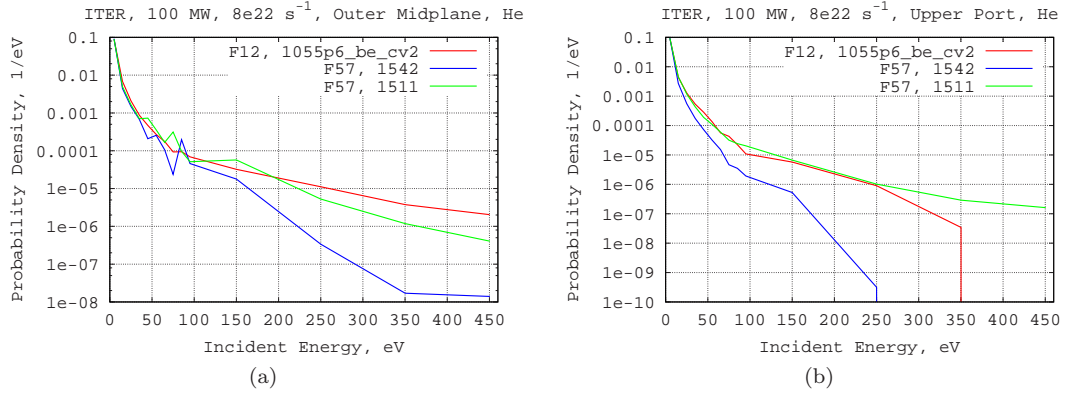


Figure 25: Comparing incident energy spectra of He at a) equatorial port and b) upper port for old (F12) and new reference (F57) ITER magnetic configuration

vanishes at low density.

7 Appendix B: EIRGRID and EIRMAP data format and libraries

7.1 General structure

Modules and libraries:

eirgrid.f: (module) data structure for grids (object **EIR_GRID**) and its generic methods;

eirmap.f: (module) data structure for mappings (object **EIR_MAP**) and its generic methods;

eirgrid_lib.f: (module) explicit interfaces to all subroutines;

eirgrid_geom.f: library of geometrical primitives;

eirgrid_interf.f: library of interfaces to the grid-type specific routines;

Libraries of the grid-type specific routines:

eirgrid_torgrid.f: EIRENE 2D toroidal grid;

Libraries of the problem specific routines:

eirgrid_b2_create.f: creating grid object out of B2 grid;

eirgrid_tria_create.f: creating grid object out of EIRENE triangular grid;

eirgrid_addsurf_create.f: creating grid object out of EIRENE additional surfaces;

7.2 EIRGRID object (module eirgrid.f)

7.2.1 EIRGRID: data

The data-structure is defined in the data-type **EIR_GRID** . Each grid is defined as a set of cells. In turn, the cells consist of edges. Edges refer to the coordinates of the points which define their actual location. An example is shown in Figure 26. Here “coordinates of the points” can be any numerical parameters which define edges. In general, they must not be coordinates of any geometrical points.

Variables and dimensions:

MAXDIM: maximum number of coordinates;

TYPE: index of the grid type;

DESCRIPTION: string with human readable description of the grid;

NCELLS: number of cells;

NEDGES: number of edges;

LEDGESS: length of array EDGES;

PDIM: number of point indices required to define one point;

EDIM: number of points required to define one edge;

GDIM: dimension of the grid (2: 2D, 3: 3D);

NPOINTS(MAXDIM): lengths of the arrays with point coordinates **X?**;

UNIT2SI(MAXDIM): transition factor to SI units (meter or radian);

UNITDESCRIPT(MAXDIM): string with human readable units for each coordinate.

Arrays which define the grid:

EDGES(LEDGES): indices of edges belonging to each cell;

IEDGESS(NCELLS): cell **I** starts in array **EDGES** at the index **IEDGESS(I)**;

IEDGESE(NCELLS): ... and finishes at the index **IEDGESE(I)**;

CELLS(2,NEDGES): indices of cells (or edges: for teleportation) for each edge;

EDGTAG(NEDGES): tags of the edges (to define properties etc.);

CELLTAG(NCELLS): tags of the cells (to define regions etc.);

POINTS(PDIM,EDIM,NEDGES): indices of points which describe each edge;

X?(NPOINTS(?)): coordinates of the points (real numbers);

Arrays with extra information:

SEDGES(NEDGES) surface areas of the edges;

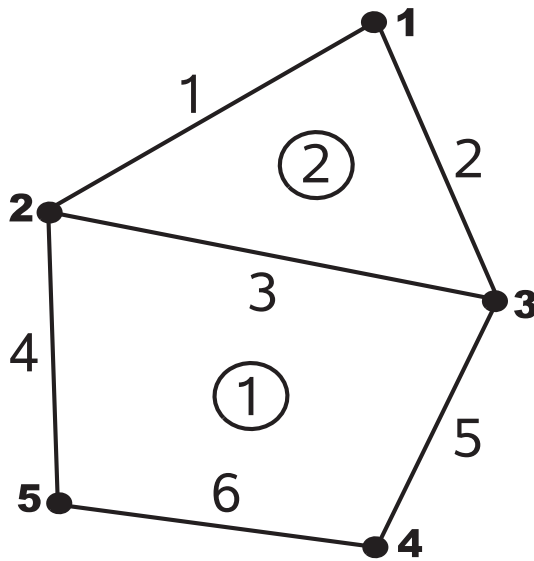
VCELLS(NCELLS) cell volumes;

XC(GDIM,NCELLS) coordinates of the cell centers;

XN(GDIM,NEDGES) coordinates of the edge normals;

ISCONVEX(NCELLS) logical variable, **.TRUE.** if the cell is convex and **.FALSE.** otherwise

Functions used to calculate these variables are grid-type specific, see below.



```

NCELL=2; NEDGES=6; LEDGESS=7
PDIM=1; EDIM=2; NPOINTS(1)=5
!CELL 1
IEDGESS(1)=1; IEDGESS(1)=4
EDGES(1:4)=(/3, 4, 5, 6/)
!CELL 2
IEDGESS(2)=5; IEDGESS(2)=7
EDGES(5:7)=(/1, 2, 3/)
!EDGES
CELLS(1,1)=2; CELLS(2,1)=0
CELLS(1,2)=2; CELLS(2,2)=0
CELLS(1,3)=2; CELLS(2,3)=1
CELLS(1,4)=1; CELLS(2,4)=0
CELLS(1,5)=1; CELLS(2,5)=0
CELLS(1,6)=1; CELLS(2,6)=0
POINTS(1,1,1)=1; POINTS(1,2,1)=2
POINTS(1,1,2)=1; POINTS(1,2,2)=3
POINTS(1,1,3)=2; POINTS(1,2,3)=3
POINTS(1,1,4)=2; POINTS(1,2,4)=5
POINTS(1,1,5)=3; POINTS(1,2,5)=4
POINTS(1,1,6)=4; POINTS(1,2,6)=5

```

Figure 26: An example of a grid and its description

7.2.2 EIRGRID: methods

All subroutines which work with object `EIR_GRID` are named `EIR_GRID...`. Subroutines of the module `EIRGRID` are called “the logical level routines”. They are valid for all grid types. This module contains:

EIR_GRID_ALLOCATE: subroutine to allocate the grid object;

EIR_GRID_ALLOCATE_EDGES: allocating arrays which depend on `NEDGES`;

EIR_GRID_ALLOCATE_CELLS: allocating arrays which depend on `NCELLS`;

EIR_GRID_ALLOCATE_POINTS: allocating arrays which depend on `NPOINTS`;

EIR_GRID_DEALLOCATE: subroutine to deallocate the grid object;

EIR_GRID_DEALLOCATE_EDGES: de-allocating arrays which depend on `NEDGES`;

EIR_GRID_DEALLOCATE_CELLS: de-allocating arrays which depend on `NCELLS`;

EIR_GRID_DEALLOCATE_POINTS: de-allocating arrays which depend on `NPOINTS`;

EIR_GRID_WRITE: subroutine which stores grid object in a file;

EIR_GRID_READ: subroutine which reads grid object from a file;

EIR_GRID_COPY: subroutine which creates a copy of the grid object.

EIR_GRID_COMP: subroutine which compares two grid objects;

EIR_GRID_EXIST: function which returns `.TRUE.` if grid object is allocated;

EIR_GRID_CONSISTENCY: checking the grid consistency;

EIR_GRID_COMBINE: combining two grid objects into one;

EIR_GRID_CREATE_CELLS: generating the table of cells from the table of edges;

Some dimensions in the call of `EIR_GRID_ALLOCATE` may be `<0`. In this case the allocation of the corresponding arrays is skipped. But the grid object is considered to be existing only if all its “obligatory arrays” (arrays which define the grid in Subsection 7.2.1) are allocated. Only in this case `EIR_GRID_EXIST` returns `.TRUE.`

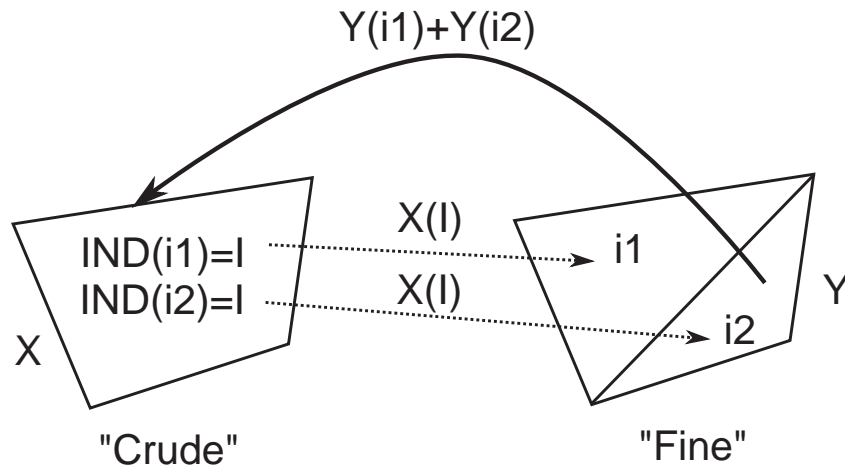


Figure 27: The principle of the mapping between two grids

7.3 EIRMAP object (module eirmap.f)

EIRMAP defines mapping of the “fine” grid into “crude” grid. Each cell of the “crude” grid contains one or more cells of the “fine” grid (definition). Here the term “cell” has a logical meaning: it can correspond either to a grid cell or to an edge. See Figure 27. This structure intentionally does not support mixed cases: when some cells of grid A contain several cells of grid B, but at the same time some cells of grid B contain several cells of grid A. This situation is forbidden.

7.3.1 EIRMAP: data

NS(2,MAXNDF): first and last cell index on the fine grid for each dimension;

NDF: number of dimensions of fine grid;

NDC: number of dimensions of crude grid;

NULL: marker for the cells of fine grid which are not connected to any cell of the crude grid;

DESCRIPTION: a string with human-readable description of the grid;

IND1D(NDF, NF(1,1):NF(2,1)): $IND(J, I)$ is the index of the cell of crude grid (corresponding to the dimension J) which contains cell I of the fine grid, this array is used if $NDF.EQ.1$;

IND2D(NDF, NF(1,1):NF(2,1), NF(1,2):NF(2,2)): $IND(J, IX, IY)$ is the index of the cell of crude grid (corresponding to the dimension J) which contains cell IX, IY of the fine grid, this array is used if $NDF.EQ.2$;

MAXNDF is a constant which defines maximum dimensionality of the fine grid.

7.3.2 EIRMAP: methods

EIR_MAP_ALLOCATE : allocating mapping table;

EIR_MAP_DEALLOCATE : de-allocating mapping table;

EIR_MAP_EXIST : function which returns **.TRUE.** if mapping exist and **.FALSE.** otherwise;

EIR_MAP_CHECK : checking correctness of the mapping object;

EIR_MAP_WRITE : saving mapping in a file;

EIR_MAP_READ : reading mapping from a file;

EIR_MAP_CRUDE_TO_FINE : map data from crude to fine grid;

EIR_MAP_FINE_TO_CRUDE : map data from fine to crude grid;

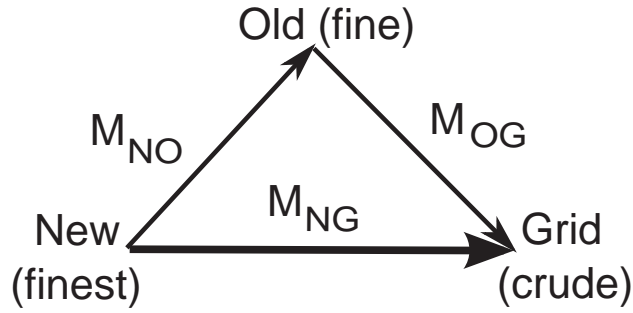


Figure 28: Diagram explaining action of the subroutine EIR_MAP_CONV

EIR_MAP_COPY : making a copy of the mapping object;

EIR_MAP_CONV : converting mapping object to the new finer grid.

EIR_MAP_CRUDE_TO_FINE and **EIR_MAP_FINE_TO_CRUDE** are generic names for the subroutines written for each combination of NDF and NDC.

EIR_MAP_CRUDE_TO_FINE assumes that the variable is constant in the cell of the crude grid:

$$I_{fine} \in I_{crude} : X_{fine}(I_{fine}) = X_{crude}(I_{crude})$$

EIR_MAP_FINE_TO_CRUDE assumes that the variables are additive:

$$i_{fine} \in I_{crude} : X_{crude}(I_{crude}) = \sum_{i_{fine}} X_{fine}(i_{fine})$$

Subroutine **EIR_MAP_CONV** converts mapping M_{OG} of the fine grid O (“Old”) onto crude grid G (“Grid”) into mapping M_{NG} of the grid N (“New”) onto G . N must be finer than O , M_{NO} is the given mapping of N onto O . See Figure 28. Note that dimensionality of the crude grid in M_{NO} must be equal to the dimensionality of the fine grid in M_{OG} .

7.4 Grid-type specific routines (eirgrid_interf.f)

File **eirgrid_interf.f** contains interfaces to the grid-type specific routines:

EIR_GRID_CHECK : checking the grid integrity;

EIR_GRID_AREAS : calculating edge areas;

EIR_GRID_VOLUMES : calculating cell volumes;

EIR_GRID_CENTER : calculating cell centers;

EIR_GRID_NORM : calculating edge normals;

EIR_GRID_ISCONVEX : marks convex cells;

EIR_GRID_ATTACH : finds common elements of two grids and attaches them to each other;

EIR_GRID_MAPEDGES : finds edges of one grid which overlap with edges of another grid;

The routines in this list are also called “the geometrical level routines“. They have to be implemented separately for each individual grid type (2D grid, 3D grid etc.).

7.5 Subroutines which create a grid object

EIR_GRID_READ_TRIA: reading triangular grid from files **fort.33-35**;

EIR_GRID_TRIA_CREATE: converting EIRENE representation of triangular grid into grid object;

EIR_GRID_TRIA_B2MAP: writing a mapping of cells from B2 grid to triangular grid using information from **fort.35**;

EIR_GRID_SAVE_TRIA: saving grid object as an EIRENE triangular grid (if possible);

EIR_GRID_READ30: reading B2 grid from `fort.30`;

EIR_GRID_B2_CREATE: converting B2 representation of its grid into grid object;

EIR_GRID_ADDSURF_CREATE: creating a grid object out of additional surfaces.

8 Appendix C: Grid generator COREGRID

8.1 Theoretical background

The program COREGRID generates the EIRENE grid in the central (core) zone inside the core boundary of the B2 grid (without X-point and separatrix). The grid is aligned along magnetic surfaces $\Psi = const$ where Ψ is the poloidal magnetic flux function. The grid generation involves the following steps:

1. Reading $\Psi_{i,j}$, r_i , z_j from the equilibrium file (*.eq)
2. Reading outer grid boundary (OGB) from the B2 grid file (fort.30)
3. Finding O-point there $\partial\Psi/\partial r = \partial\Psi/\partial z = 0$
4. Defining Ψ_l for radial surfaces
5. Constructing radial surfaces as $\Psi = const = \Psi_l$
6. Defining grid points as intersections of radial and poloidal surfaces
7. Triangularizing the grid and saving it in EIR_GRID format

The function $\Psi_{i,j}$ is defined on a cartesian grid, r_i , z_j are the major radius and vertical coordinate respectively, $i \in [1, n_r]$, $j \in [1, n_z]$. Grid cell (i, j) is bounded between the nodes (i, j) , $(i+1, j)$, $(i, j+1)$, $(i+1, j+1)$, Figure 29. The cell indices lie therefore in the range $i \in [1, n_r - 1]$, $j \in [1, n_z - 1]$. The algorithm is based on the simple bi-linear interpolation of Ψ within each cell:

$$\Psi_{i,j}(r, z) = \Psi_{i,j} + \Psi_{i,j}^r (r - r_i) + \Psi_{i,j}^z (z - z_j) + \Psi_{i,j}^c (r - r_i)(z - z_j) \quad (2)$$

Here:

$$\Psi_{i,j}^r = \frac{\Psi_{i+1,j} - \Psi_{i,j}}{r_{i+1} - r_i}; \quad \Psi_{i,j}^z = \frac{\Psi_{i,j+1} - \Psi_{i,j}}{z_{j+1} - z_j}; \quad \Psi_{i,j}^c = \frac{\Psi_{i+1,j+1} + \Psi_{i,j} - \Psi_{i+1,j} - \Psi_{i,j+1}}{(r_{i+1} - r_i)(z_{j+1} - z_j)}$$

The range of indices on which $\Psi_{i,j}^r$ is defined is $i \in [1, n_r - 1]$, $j \in [1, n_z]$; $\Psi_{i,j}^z$: $i \in [1, n_r]$, $j \in [1, n_z - 1]$; $\Psi_{i,j}^c$: $i \in [1, n_r - 1]$, $j \in [1, n_z - 1]$. It is readily seen that:

$$\Psi(r_i, z_j) = \Psi_{i,j} = \Psi_{i,j}$$

$$\Psi(r_{i+1}, z_j) = \Psi_{i,j} + (\Psi_{i+1,j} - \Psi_{i,j}) = \Psi_{i+1,j}$$

$$\Psi(r_i, z_{j+1}) = \Psi_{i,j} + (\Psi_{i,j+1} - \Psi_{i,j}) = \Psi_{i,j+1}$$

$$\Psi(r_{i+1}, z_{j+1}) = \Psi_{i,j} + (\Psi_{i+1,j} - \Psi_{i,j}) + (\Psi_{i,j+1} - \Psi_{i,j}) + (\Psi_{i+1,j+1} + \Psi_{i,j} - \Psi_{i+1,j} - \Psi_{i,j+1}) = \Psi_{i+1,j+1}$$

The O-point is found as a grid node which fullfills the following conditions:

1. $i \in [1, n_r - 1]$, $j \in [1, n_z - 1]$
2. $\Psi_{i,j}^r \cdot \Psi_{i-1,j}^r \leq 0$ and $\Psi_{i,j}^z \cdot \Psi_{i,j-1}^z \leq 0$
3. The point lies inside OGB

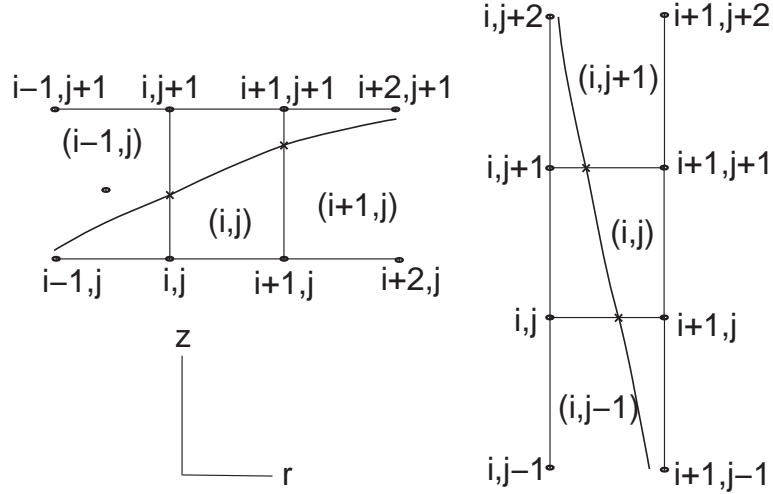


Figure 29

There must be only one O-point inside OGB, otherwise the code indicates incorrect input. The applied algorithm is very primitive. In principle, one could use higher order approximations for $\Psi(r, z)$ and look for the point of extremum inside each cell.

The radial surfaces are defined by either defining explicitly Ψ_l or by defining distribution over the minor radius and then finding Ψ_l for each radial distance.

Radial surfaces ($\Psi = \text{const}$) are defined as sequences of cells (i_l, j_l) . In each (i_l, j_l) the following equation defines a piece of magnetic surface:

$$\Psi_{i,j}(r, z) = \Psi_l \quad (3)$$

A cell (i, j) is added to the sequence (i_l, j_l) if the curve $\Psi_{i,j}(r, z) = \Psi_l$ has exactly two intersections with the edges of the cell (i, j) . The number of intersections which is neither 0 nor 2 would mean an error in the algorithm.

Intersection with vertical edges is found by solving the equations $\Psi_{i,j}(r_i, z) = \Psi_l$ and $\Psi_{i,j}(r_{i+1}, z) = \Psi_l$. According to Equation (2) $\Psi_{i,j}(r_i, z) = \Psi_l$ yields:

$$\Psi_{i,j} - \Psi_l + \Psi_{i,j}^z (z - z_j) = 0 \quad (4)$$

Second equation $\Psi_{i,j}(r_{i+1}, z) = \Psi_l$ gives:

$$\Psi_{i,j} - \Psi_l + \Psi_{i+1,j} - \Psi_{i,j} + \frac{\Psi_{i,j+1} - \Psi_{i,j}}{z_{j+1} - z_j} (z - z_j) + \frac{\Psi_{i+1,j+1} + \Psi_{i,j} - \Psi_{i+1,j} - \Psi_{i,j+1}}{z_{j+1} - z_j} (z - z_j) = 0$$

Or:

$$\Psi_{i+1,j} - \Psi_l + \Psi_{i+1,j}^z (z - z_j) = 0 \quad (5)$$

Intersection points have therefore the following coordinates:

$$\left(r_i, z = \frac{\Psi_l - \Psi_{i,j}}{\Psi_{i,j}^z} + z_j \right); \quad \left(r_{i+1}, z = \frac{\Psi_l - \Psi_{i+1,j}}{\Psi_{i+1,j}^z} + z_j \right)$$

The cell edge is intersected if $z_j \leq z \leq z_{j+1}$.

Similarly for horizontal edges. $\Psi_{i,j}(r, z_j) = \Psi_l$ leads to:

$$\Psi_{i,j} - \Psi_l + \Psi_{i,j}^r (r - r_i) = 0 \quad (6)$$

$\Psi_{i,j}(r, z_{j+1}) = \Psi_l$ yields:

$$\Psi_{i,j} - \Psi_l + \frac{\Psi_{i+1,j} - \Psi_{i,j}}{r_{i+1} - r_i} (r - r_i) + \Psi_{i,j+1} - \Psi_{i,j} + \frac{\Psi_{i+1,j+1} + \Psi_{i,j} - \Psi_{i+1,j} - \Psi_{i,j+1}}{r_{i+1} - r_i} (r - r_i) = 0$$

Or:

$$\Psi_{i,j+1} - \Psi_l + \Psi_{i,j+1}^r (r - r_i) = 0 \quad (7)$$

The coordinates of the intersection points:

$$\left(r = \frac{\Psi_l - \Psi_{i,j}}{\Psi_{i,j}^r} + r_i, z_j \right); \quad \left(r = \frac{\Psi_l - \Psi_{i,j+1}}{\Psi_{i,j+1}^r} + r_i, z_{j+1} \right)$$

The cell edge is intersected if $r_i \leq r \leq r_{i+1}$.

It is necessary to prove that coordinates of the intersection points calculated using $\Psi_{i,j}(r, z)$ in the neighboring cells match each other. In order to do this four cases are considered.

Case 1, flux surface intersects the line $r = r_i$, see Figure 29, left. In the cell $(i-1, j)$ Equation (3) reads:

$$\Psi_{i-1,j} - \Psi_l + \Psi_{i-1,j}^r (r - r_{i-1}) + \Psi_{i-1,j}^z (z - z_j) + \Psi_{i-1,j}^c (r - r_{i-1})(z - z_j) = 0$$

At $r = r_i$ this yields:

$$\Psi_{i-1,j} - \Psi_l + \Psi_{i,j} - \Psi_{i-1,j} + \frac{\Psi_{i-1,j+1} - \Psi_{i-1,j}}{z_{j+1} - z_j} (z - z_j) + \frac{\Psi_{i,j+1} + \Psi_{i-1,j} - \Psi_{i-1,j+1} - \Psi_{i,j}}{z_{j+1} - z_j} (z - z_j) = 0$$

$$\Psi_{i,j} - \Psi_l + \Psi_{i,j}^z (z - z_j) = 0 \quad (8)$$

Equation (8) is exactly the same as Equation (4), therefore, coordinates of the intersection calculated in the cells (i, j) and $(i-1, j)$ match.

Case 2, flux surface intersects the line $r = r_{i+1}$, see Figure 29, left. In the cell $(i+1, j)$ Equation (3) reads:

$$\Psi_{i+1,j} - \Psi_l + \Psi_{i+1,j}^r (r - r_{i+1}) + \Psi_{i+1,j}^z (z - z_j) + \Psi_{i+1,j}^c (r - r_{i+1})(z - z_j) = 0$$

At $r = r_{i+1}$ this yields:

$$\Psi_{i+1,j} - \Psi_l + \Psi_{i+1,j}^z (z - z_j) = 0 \quad (9)$$

Equation (9) is exactly the same as Equation (5), therefore, coordinates of the intersection calculated in the cells (i, j) and $(i+1, j)$ match.

Case 3, flux surface intersects the line $z = z_j$, see Figure 29, right. In the cell $(i, j-1)$ Equation (3) reads:

$$\Psi_{i,j-1} - \Psi_l + \Psi_{i,j-1}^r (r - r_i) + \Psi_{i,j-1}^z (z - z_{j-1}) + \Psi_{i,j-1}^c (r - r_i)(z - z_{j-1}) = 0$$

At $z = z_j$ this yields:

$$\Psi_{i,j-1} - \Psi_l + \frac{\Psi_{i+1,j-1} - \Psi_{i,j-1}}{r_{i+1} - r_i} (r - r_i) + \Psi_{i,j} - \Psi_{i,j-1} + \frac{\Psi_{i+1,j} + \Psi_{i,j-1} - \Psi_{i+1,j-1} - \Psi_{i,j}}{r_{i+1} - r_i} (r - r_i) = 0$$

$$\Psi_{i,j} - \Psi_l + \Psi_{i,j}^r (r - r_i) = 0 \quad (10)$$

Equation (10) is exactly the same as Equation (6), therefore, coordinates of the intersection calculated in the cells (i, j) and $(i, j-1)$ match.

Case 4, flux surface intersects the line $z = z_{j+1}$, see Figure 29, right. In the cell $(i, j+1)$ Equation (3) reads:

$$\Psi_{i,j+1} - \Psi_l + \Psi_{i,j+1}^r (r - r_i) + \Psi_{i,j+1}^z (z - z_{j+1}) + \Psi_{i,j+1}^c (r - r_i)(z - z_{j+1}) = 0$$

At $z = z_{j+1}$ this yields:

$$\Psi_{i,j+1} - \Psi_l + \Psi_{i,j+1}^r (r - r_i) = 0 \quad (11)$$

Equation (11) is exactly the same as Equation (7), therefore, coordinate of the intersection calculated in the cells (i, j) and $(i, j+1)$ match.

Strictly speaking poloidal surfaces are the surfaces perpendicular to $\Psi = \text{const}$ magnetic surfaces. Since the COREGRID is intended first of all to produce grids for a neutral transport code, currently a simplified approach is used. The poloidal surfaces are defined as straight rays drawn from the points of OGB to the O-point: proper poloidal angle as poloidal coordinate.

In general, intersection point of the surface $\Psi_{i,j}(r, z) = \Psi_l$ and the straight line which is defined as a parametric equation: $r = r_0 + v_r t, z = z_0 + v_z t$, is found by solving the following equation:

$$\Psi_{i,j} - \Psi_l + \Psi_{i,j}^r (r_0 - r_i + v_r t) + \Psi_{i,j}^z (z_0 - z_j + v_z t) + \Psi_{i,j}^c (r_0 - r_i + v_r t)(z_0 - z_j + v_z t) = 0$$

Or:

$$At^2 + Bt + C = 0; \quad t = \frac{-B \pm \sqrt{B^2 - 4AC}}{2A} \quad (12)$$

Where:

$$A = \Psi_{i,j}^c v_r v_z; \quad B = \Psi_{i,j}^r v_r + \Psi_{i,j}^z v_z + \Psi_{i,j}^c [v_z (r_0 - r_i) + v_r (z_0 - z_j)]$$

$$C = \Psi_{i,j} - \Psi_l + \Psi_{i,j}^r (r_0 - r_i) + \Psi_{i,j}^z (z_0 - z_j) + \Psi_{i,j}^c (r_0 - r_i) (z_0 - z_j)$$

In the case in question $r_0 = r_k$, $z_0 = z_k$, $v_r^k = r_O - r_k$ and $v_z^k = z_O - z_k$. Here k is the index of points on the OGB, (r_O, z_O) are coordinates of the O-point. It must be $t > 0$ and the intersection points $r = r_k + (r_O - r_k)t$, $z = z_k + (z_O - z_k)t$ must belong to the interval $r_k < r < r_O$, $z_k < z < z_O$ or $r_O < r < r_k$, $z_O < z < z_k$.

To get an accurate solution of the quadratic equation (12) the following trick is used. Equation (12) is multiplied with the sign of B . This ensures that $B \geq 0$. The root with “plus” is transformed as follows:

$$t = \frac{-B + \sqrt{B^2 - 4AC}}{2A} = \frac{(-B + \sqrt{B^2 - 4AC})(B + \sqrt{B^2 - 4AC})}{2A(B + \sqrt{B^2 - 4AC})} = \frac{-2C}{B + \sqrt{B^2 - 4AC}} \quad (13)$$

It is preferable to use Formula (13) instead of (12) because the former is more accurate when $|4AC| \ll B^2$: Formula (13) avoids calculating of the small difference between two large positive numbers. It is readily seen that (13) yields a positive solution if $C < 0$. Second root: $t = (-B - \sqrt{B^2 - 4AC})/2A$ yields a positive solution if $A < 0$.

8.2 Technical description

Technically COREGRID consists of two parts: module CORENODES which performs calculations, and interface COREGRID which prepares input for them. Subroutine CORENODES_INIT initializes CORENODES with input: arrays Ψ , r , z . This subroutine also pre-calculates all variables required for interpolation (Ψ^r , Ψ^z , Ψ^c and further variables which can optimize interpolation). After initialization the values of Ψ -function on any set of points inside the computational grid can be calculated with CORENODES_INTERP. Subroutine CORENODES_RUN calculates the grid nodes starting from the given Outer Grid Boundary on the magnetic surfaces defined by Ψ_l . This subroutine also needs coordinates of the O-point as input.

CORENODES executes the following sequence of operations:

1. COREGRID_READINPUT: reading the input file `coregrid.parameters`;
2. COREGRID_READ_EQU: reading magnetic equilibrium $\Psi(r, z)$
3. COREGRID_READ_OGB: defining Outer Grid Boundary (OGB);
4. CORENODES_INIT: initializing interpolation routines;
5. COREGRID_OPOINT: finding O-point r_O, z_O ;
6. COREGRID_PSIL_SET: defining radial surfaces $\Psi = \Psi_l$;
7. CORENODES_RUN: calculating the coordinates of the grid nodes;
8. COREGRID_CHECK: check that the grid nodes lie on the $\Psi = \Psi_l$ surfaces;
9. COREGRID_SAVE: converting the set of grid nodes into grid object and save it on disk.

The list of input variables and their description can be found in MODULE COREGRID_INPUT. OGB is normally the radial surface number B2IY of the B2 grid. This latter is defined in `fort.30`. The surface must be closed. O-point must be unique inside OGB, otherwise the code stops with error message. Radial surfaces are defined either by prescribing values of Ψ , or normalized Ψ (equals 1 at O-point and equals 0 at OGB) or by prescribing the normalized minor radius at the Outer Midplane (1 at O-point and 0 at OGB). Values of Ψ_l must be monotonic and must lie between values of Ψ at OGB and O-point. Flag `FILLO=.TRUE.` ensures that triangles are added between last $\Psi = \Psi_l$ surface and the O-point, otherwise this space is left empty. The generated grid object contains the triangular grid.

9 Appendix D: The spectrum calculation option in EIRENE

9.1 Technical description

The code related to the spectrum calculation can be found mainly in three subroutines: `CALC_SPECTRUM`, `STATIS_SPC`, `OUTSPEC` and a new datatype and arrays in module `CESTIM`. Other involved subroutines are: `INPUT`, `PARMMOD`, `LOCATE`, `ESCAPE`, `FOLNEUT`, `FOLION`, `OUTEIR`. The corresponding pieces of code are marked by the comment `SVK`.

The main subroutine which updates the calculated spectrum is `CALC_SPECTRUM`. It is called from `LOCATE`, `ESCAPE`, `FOLNEUT` and `FOLION`. The spectrum is stored in the array `SMESTL`, type `EIRENE_SPECTRUM`. The data type and array are defined in `CESTIM`. To calculate the spectrum a selected interval for the variable in question (e.g. the particle kinetic energy) is divided into a set of bins. The current algorithm supports only equidistant division because this is the easiest case for calculating the bin's index:

$$IB = (EB - SPCMIN) \cdot SPCDELI + 1; \quad SPCDELI = \left[\frac{NSPC}{(SPCMAX - SPCMIN)} \right] \quad (14)$$

Here `EB` is the variable in question, `SPCMAX` and `SPCMIN` are the ends of the interval and `NSPC` is the number of bins between `SPCMIN` and `SPCMAX`. The spectrum is stored in array `SMESTL%SPC`. If `EB` is smaller than `SPCMIN` or greater than `SPCMAX`, then the update is made for bins `SPC(0)` and `SPC(NSPC+1)` respectively. For surface spectra only the incident particles are taken into account (no reflected particles).

The parameters of the spectrum to be calculated are read from Block 10F in the input file (subroutine `INPUT`). Subroutine `MCARLO` contains the code which updates `SMESTL` (sum over all strata) from `ESTIML`: this is an object of the same type but containing estimate from only current stratum. The standard deviation for spectrum is calculated by subroutine `STATIS_SPC`. The entries of this subroutine (`STATS0_SPC`, `STATS1_SPC`, `STATS2_SPC`) are called from `MCARLO`. The variance is saved in the array `SMESTL%SGM` (`SMESTL%SGV` is the expectation). `ESTIML` is rescaled in subroutines `SCAL_SURFACE_TALLIES`, `SCAL_VOLAV_TALLIES` and `SCAL_TALLIES`. Other related files are: `PARMMOD` (variable `NADSPC`: the number of spectra to consider) and `OUTEIR` (call for `OUTSPEC`: the output of the calculated spectrum).

For the present project these options were updated in order to be able to calculate an angular distribution for the surface spectrum. For this purpose the arrays `SPC`, `SDV`, `SGM` are made 2D in order to be able to store both the energy and angular spectrum. The update of the angular bins is done in the same way as for the energy (Formula 14). The angle of incidence is calculated as the angle between surface normal `CRTX`, `CRTY`, `CRTZ` and the velocity vector `VELX`, `VELY`, `VELZ` of the incident particle. The update is made only if the test particle is incident in the direction of the surface normal: that is, the angle is smaller than 90^0 , and if the particle statistical weight is positive. Normally the weight must be positive for the angle $<90^0$ and negative otherwise. If it is not the case, then the message: "WARNING: WT AND AINC HAVE DIFFERENT SIGNS. POSSIBLE ERROR IN SPECTRUM" is printed. For the reason of optimization EIRENE does not calculate the surface normal vector for the transparent surfaces with `ILIIN`<0. Therefore, for transparent diagnostic surfaces with `ILIIN`=-3 this calculation is made in `CALC_SPECTRUM` using a piece of code taken from `ADDCOL` (internal subroutine `GET_SURF_NORMAL`).

9.2 Instruction for Users: Input and Output

The number of spectra to be calculated has to be specified in Block 10, variable `NADSPC`. The parameters of spectrum for each spatial location (volume cell or surface element) are specified in block 10F. The input card reads:

```
READ (IUNIN,'(12I6)') ISPSRF, IPTYP, IPSP, ISPTYP, NSPS, ISRFCLL, IDIREC
READ (IUNIN,'(6ES12.4)') SPCMN, SPCMX, SPC_SHIFT, SPCPLT_X, SPCPLT_Y,
SPCPLT_SAME
IF (IDIREC /= 0) THEN
READ (IUNIN,'(6ES12.4)') SPCVX, SPCVY, SPCVZ
END IF
```

Here:

- `ISPSRF` is the index of cell (for volume spectrum) or of the surface element (surface spectrum). Negative values correspond to Non-Default Standard Surfaces.

- IPTYP is the type of species (1: atom, 2: molecule, 3: test ion, 0: photon).
- IPSP is the index of the species of this type.
- ISPTYP is the type of spectrum (1: normal spectrum, 2: energy weighted, 3: velocity weighted).
- NSPS is the number of bins for incident energy.
- ISRFCLL: 0 stands for surface spectrum and 1 for volume spectrum.
- IDIREC controls the additional input (see below).
- SPCMN, SPCMX are the minimum and maximum of the energy range.

Other variables are not in use yet. Only the calculation of the energy distribution function (not the velocity distribution) has been tested so far.

If IDIREC \neq 0, then in case of volume spectrum SPCVX, SPCVY, SPCVZ are the coordinate of the direction for which the velocity distribution will be calculated. For the surface spectrum it is the input data for angular distribution:

- SPCVX=AMIN minimum angle (default 0);
- SPCVY=AMAX maximum angle (default 90°)
- SPCVZ=NSAN number of angular bins (default 0)

If NSAN=0 then the angular dependence is not calculated but only test particles with incident angle A laying between AMIN and AMAX are taken into account in the spectrum. If NSAN>0, then the true angular distribution is calculated. In case NSAN=1 the particles with A<AMIN will be put into the bin 0 and the particles with A>AMAX will be put into the bin 2.

All the output of the calculated spectrum and related data is made from the subroutine OUTSPEC. One has to refer to this subroutine in case of any queries concerning the output specification. Each spectrum is printed into a separate file "spectra.X" where X is the number of spectrum in the input. Two formats are possible: with and without angular distribution. An output without angular distribution has 4 columns:

1. subsequent number of the field (for human reader);
2. coordinates of the bin boundaries (in eV), starting from 0, then SPCMN etc.;
3. coordinates of the bin centres (may be more convenient for plotting);
4. probability density for each bin: particles with energy less than SPCMN in the first row, first bin in the second row... etc.

The last column (position 4) contains the *normalized distribution* (divided by the integral!). The units are 1/eV (probability density). That means that the particle flux in each bin is divided by the size of this bin (energy difference), except for the last bin which corresponds to the interval from SPCMX to infinity. The integral over the probability density must be one. If the statistics for the spectrum is switched on (Block 9, "CARDS FOR EMPIRICAL STANDARD DEVIATION", NSIGL_SPC>0), then a 5th column will appear. It contains the relative standard deviation for each bin.

The output with angular distribution is enforced for surface spectra if NSAN>0. The first line has the following format:

```
NSAN 0.0 0.0 0.0 DANG(:)
```

Here NSAN is the number of angular bins and DANG are the coordinates of the bin boundaries (in Radians): from AMIN to AMAX. The succeeding lines have the same structure as in case of the output without angular dependence. The first three columns are the indices, the energy bin boundaries and the central value of the energy bin. The next NSAN+2 columns contain the probability density for each angular bin. The first column corresponds to the angles from 0 to AMIN, then the first bin etc. The last column stands for the angles from AMAX to 90°. If the statistics is switched on, then the first line looks as follows:

```
NSAN 0.0 0.0 0.0 DANG(:) 0.0 0.0 DANG(:)
```

The columns with the probability density are followed by NSAN+2 columns with relative standard deviation. As in the case without angular distribution, the printed distribution is *normalized* by the integral. The units are 1/eV/Rad: that is, the flux calculated for each angular bin is divided by the size of this bin (in addition to the energy interval) to get the probability density. The 2D integral over energy and angle has to be equal one.

General information for the all spectra calculated is printed into a separate file "spectra.h". Each record contains the following information: the type of species, the type of spectrum, energy and angular range. For surface spectra some lines labeled as "ADDITIONAL INFORMATION" are also printed:

- INCIDENT FLUX DENSITY is the flux from array POTAT (atoms), POTML (molecules), POTIO (test ions), POTPL (bulk ions) or POTPHT (photons) divided by the surface area and transformed from Ampere to 1/cm²/s.
- INCIDENT ENERGY DENSITY is the energy flux EOTAT (atoms), EOTML (molecules), EOTIO (test ions), EOTPL (bulk ions) or EOTPHT (photons) divided by the surface area, W/cm².
- AVERAGE ENERGY is the ratio "INCIDENT ENERGY DENSITY" / "INCIDENT FLUX DENSITY", eV per particle.

The surface area is taken from array SAREA. For surfaces with ILIIN=-3 the emitted flux PRFAAT or PRFMML or PRFIIIO or PRFPHPT (depending of the particle type) is subtracted from "INCIDENT FLUX DENSITY". This correction is necessary because in this configuration of EIRENE for the surfaces with ILIIN=-3 arrays POTAT etc. contain the net flux but not the incident flux. The same correction is done for the "INCIDENT ENERGY DENSITY": ERFAAT or ERFMML or ERFIIIO or ERFPHPT are subtracted.

The field "INTEGRAL OF SPECTRUM" is the total flux (Ampere) of particles which were taken into account in calculating the spectrum. "FLUX DENSITY" is this flux, divided by the surface area. This quantity has to be always equal to "INCIDENT FLUX DENSITY" for the spectrum without angular dependence or for the spectrum with NSAN>0.

9.3 Test problems

The following test problem was considered. A 2D slab filled with Deuterium plasma with temperature 1 eV and density 10¹³ cm⁻³. The size of the slab is 100 by 100 cm. Its boundaries are perfectly reflecting walls (ILIIN=3). A 10 by 10 cells grid is defined in the slab. A point source of D atoms is placed in the center of the region (point X=50 cm, Y=50 cm). The source is isotropic and mono-energetic with energy 1 eV. The atoms can experience charge-exchange collisions (CX) with constant collision rate coefficient 10⁻⁸ = e^{-18.4} cm³/s and ionization (EI) with the collision rate coefficient e⁻²⁵ cm³/s. For these conditions the Mean Free Path for CX is ≈10 cm which ensures thermalization of the test particles. The CX rate is 3 orders of magnitude higher than the EI rate. Therefore, the distortion of the distribution function due to absorption is negligible and one expects that Maxwellian distribution of the test particles is established in the simulation.

The distribution functions for the incident energy and angular spectrum are calculated on the diagnostic additional surface (ILIIN=-3) parallel to the surface X=0 placed at very small distance (0.001 cm) from this surface. The theoretical distribution can be obtained by transforming the Maxwellian flux velocity distribution function:

$$f(v_x, v_y, v_z)dv_x dv_y dv_z = C v_x \exp\left(-\frac{v_x^2 + v_y^2 + v_z^2}{2mT}\right) dv_x dv_y dv_z$$

into polar coordinates. Here the axis x is perpendicular to the surface, C is the normalizing constant. Taking into account, that $v_x = v \cos \theta$ and $dv_x dv_y dv_z = v^2 \sin \theta$ ($v = \sqrt{v_x^2 + v_y^2 + v_z^2}$, θ is the polar angle between the outer surface normal and the incident velocity), the transformation yields:

$$f(v, \theta)dv d\theta = C v \cos \theta \exp\left(-\frac{v^2}{2mT}\right) v^2 \sin \theta dv d\theta$$

Replacing velocity v by the kinetic energy $E = mv^2/2$ ($dE = mv dV$) yields:

$$f(E, \theta)dE d\theta = C E \sin 2\theta \exp\left(-\frac{E}{T}\right) dE d\theta$$

The integral over the azimuthal angle (from 0 to 2π) has been hidden in constant C. This latter is found by integration over E from 0 to ∞ and over θ from 0 to $\pi/2$:

$$\int_0^{\pi/2} \sin 2\theta d\theta \int_0^{\infty} E \exp\left(-\frac{E}{T}\right) dE = \frac{1}{2} \cos 2\theta \Big|_{\pi/2}^0 \cdot \left[T^2 \left(\frac{E}{T} + 1 \right) \exp -\frac{E}{T} \right] \Big|_0^{\infty} = T^2$$

The final formula reads:

$$f(E, \theta) = \frac{E}{T^2} \sin 2\theta \exp\left(-\frac{E}{T}\right) \quad (15)$$

Test results are shown in Figure 30a. 10^5 histories are sampled, 100 bins are used for energy distribution from 0.01 to 4 eV. The angular distribution is stored in 6 bins from 15° to 75° . On the theoretical curves the coefficient $\sin 2\theta$ in Equation (15) was replaced by the average value for each bin:

$$\overline{\sin 2\theta} = \frac{1}{\theta_2 - \theta_1} \int_{\theta_1}^{\theta_2} \sin 2\theta d\theta = \frac{\cos 2\theta_1 - \cos 2\theta_2}{2(\theta_2 - \theta_1)}$$

Here θ_1 and θ_2 are the low and upper boundary of the angular bin. The angles shown in the legend in Figure 30a are the markers of the bins (an angle inside the bin, not necessarily center). The energy distribution for 20° and 75° shown in Figure 30a are the same because they correspond to the bins symmetric with respect to 45° .

One extra test was made specifically for the angular distribution. A point source of D_2 molecules is placed in front of the surface $X=0$ (coordinates $X=5$ cm, $Y=50$ cm). The emitted molecules have constant energy 1 eV. The polar angle is distributed according to the sine law (uniformly over solid angle) from 0 to 45° (the axis is parallel to the surface normal), the azimuthal angle is distributed uniformly from 0 to 360° . The molecules undergo ionization with the rate $\langle \sigma v \rangle = e^{-17} \text{ cm}^3/\text{s}$.

The distribution of the incident particles is calculated on the same Additional Surface as for the previous problem. The boundary surface is a mirror surface for molecules. The ionization mean free path is smaller than 5 cm, therefore the reflected molecules can be neglected in the analysis. In this case the angular distribution for the incident particles from the source is given by the function:

$$f(\theta) = C \sin \theta \exp\left(-\frac{R}{\cos \theta}\right), \quad R = \frac{L \langle \sigma v \rangle n}{\sqrt{2E/m}}$$

Here $\sin \theta$ takes into account the initial distribution from the source and the exponent takes into account the absorption (the path from the sources for the particles incident under bigger angle is larger, therefore the $\cos \theta$ in denominator), L is the distance between the source and the surface. The normalizing constant C is obtained by integrating $f(\theta)$ from minimum cut-off angle θ_{min} to the maximum angle θ_{max} :

$$\begin{aligned} C^{-1} &= \int_{\theta_{min}}^{\theta_{max}} \sin \theta \exp\left(-\frac{R}{\cos \theta}\right) d\theta = |t = \cos \theta| = \int_{\cos \theta_{max}}^{\cos \theta_{min}} \exp\left(-\frac{R}{t}\right) dt = \\ &= \left| \begin{array}{l} y = -\frac{R}{t} \\ dt = \frac{R}{y^2} dy \end{array} \right| = \int_{-\frac{R}{\cos \theta_{max}}}^{-\frac{R}{\cos \theta_{min}}} \frac{e^y}{y^2} dy = R \left[\text{Ei}(y) - \frac{e^y}{y} \right] \Big|_{-\frac{R}{\cos \theta_{max}}}^{-\frac{R}{\cos \theta_{min}}} \end{aligned}$$

The last integral was calculated using Integrator www.integrals.wolfram.com/index.jsp, $\text{Ei}(y) = -\int_{-x}^{\infty} \frac{e^{-t}}{t} dt$ is the Integral Exponent. The test result obtained with 10^7 histories is shown in Figure 30b. The angle incident from 0 to 75° was divided by 60 bins. The cut-off at 45° is not shown for the analytic formula.

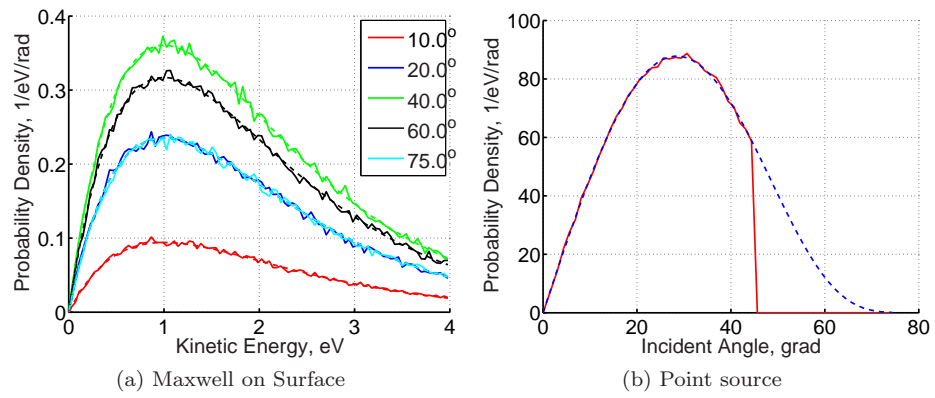


Figure 30: Results of the two test calculations described in the text. Solid lines are the calculations, dashed lines are the analytic formulas